Project No. 12-3374

Validation Experiments for Spent-Fuel Dry-Cask In-Basket Convection

Fuel Cycle Research and Development

Barton Smith
Utah State University

JC De La Garza, Federal POC
Brady Hanson, Technical POC

NEUP Nuclear Energy University Programs
U.S. Department of Energy

Final Report: Validation Experiments for Spent-Fuel Dry-Cask In-Basket Convection Project 12-3374

Barton L. Smith
Principle Investigator
Department of Mechanical and Aerospace Engineering
Utah State University
Logan, Utah 84322
barton.smith@usu.edu

ABSTRACT

This work consisted of the following major efforts:

1. Literature survey on validation of external natural convection
2. Design the experiment
3. Build the experiment
4. Run the experiment
5. Collect results
6. Disseminate results
7. Perform a CFD validation study using the results.

We note that while all tasks are complete, some deviations from the original plan were made. Specifically, geometrical changes in the parameter space were skipped in favor of flow condition changes, which were found to be much more practical to implement. Changing the geometry required new as-built measurements, which proved extremely costly and impractical given the time and funds available.

Nomenclature

A Cross-sectional area
A_s Surface area
B_r Bias error of a measured variable r
C_μ Turbulence model constant
D Experimental data
D_h Hydraulic diameter
E Validation comparison error
$\tilde{E}$ Estimated model error
g Acceleration due to gravity
h Heat transfer coefficient
I Turbulence intensity

K Pressure loss coefficient
k Turbulence kinetic energy
k_f Fluid thermal conductivity
L Characteristic length
ℓ Turbulent model mixing length
$\dot{m}$ Mass flow rate
N Number of vectors
n Number of experiments performed
Q Volume flow rate
q Heat transfer
q'' Heat flux
S Simulation solution
S_r Random error on a measured variable r
s Standard deviation
T_s Surface Temperature
T_∞ Free-stream temperature
$t_{\alpha/2,\nu}$ Quantile for t distribution with ν degrees of freedom
U_D Experimental data uncertainty
U_{input} Simulation uncertainty due to input uncertainty
U_{num} Numerical model uncertainty
U_r Uncertainty of a measured variable r
U_{val} Validation uncertainty
$U_{\bar{x}}$ Uncertainty of single mean velocity vector
$\overline{u}$ Time-averaged velocity in the x-direction
$\overline{u'u'}$ Reynolds normal stress in the x-direction
$\overline{u'v'}$ Reynolds shear stress in the xy-direction
$\overline{v}$ Time-averaged velocity in the y-direction
$\overline{v'v'}$ Reynolds normal stress in the y-direction
$\overline{w}$ Time-averaged velocity in the z-direction
$\overline{w}_{\text{bulk}}$ Average inlet velocity
$\overline{w'w'}$ Reynolds normal stress in the z-direction
x Transverse direction
y Aluminum wall-normal direction
$\overline{y}_{\text{e}}$ Estimated mean based on n experiments
y_{m} Model system response quantity
z Stream-wise direction
α Thermal diffusivity
β Coefficient of thermal expansion
ΔP Measured pressure difference
ε Turbulence dissipation rate
ε_s Surface emissivity
θ Dimensionless Temperature
ν Kinematic viscosity
ρ Fluid density
σ_x Standard deviation
$\overline{\tau}$ Turbulent shear stress
ω Specific turbulence dissipation rate

1 Introduction

There are two major thrusts of this work. Section 2 describes a Benchmark Validation Data Experiment and is based on the PhD Dissertation of Kyle Jones. Section 3 describes a validation study performed by Co-PI Robert Spall and students using the data from Section 2.

1.1 CFD Validation

The overarching purpose of this work is to provide experimental benchmark validation data of steady-state, single-phase, natural convection flow through a vertical nuclear fuel rod bundle for three-dimensional Computational Fluid Dynamics (CFD) simulations. The experimental facility, instrumentation, data acquisition system, boundary conditions (BCs) and system response quantities (SRQs) are described in detail. All inflow, BCs and SRQs are available under on the Utah State University Library's Digital Commons online database corresponding to [1]. Two flow conditions are presented here, but two additional conditions are available in the database. The geometry, BCs and SRQs are available under the same file names presented in this work. Three other benchmark cases (one forced, unheated case and two mixed convection cases with the same heat flux levels presented here) are also available for download to be used as preliminary simulations for CFD modelers. We anticipate that these cases are less challenging for CFD compared to natural convection.

The BCs and SRQs are table formatted as comma-separated values (*.csv) text files. The geometry needed to perform the simulations is included in three, widely used formats: Parasolid (*.x_t), STEP (*.stp) and Binary Stereolithography (*.stl). The files for the geometry may be downloaded in the file Geometry.zip. The BCs and SRQs for the two heat flux cases considered, 400 W/m^2 and 700 W/m^2 (referred to as Natural400 and Natural700, respectively), in this study may be downloaded in the Natural400.zip and Natural700.zip files, respectively. In each of these files, the name of the variable is presented at the column header with the units in brackets and the uncertainty for that variable is indicated by a lowercase u preceding the variable name and the standard deviation by a lowercase s. For example, the column header 'W[m/s]' is the w-velocity in units of meter per second and the column header 'uW[m/s]' is the uncertainty in the W-velocity in units of meters per second, and the column 'sW[m/s]' is the standard deviation of the w-velocity component in units of meters per second.

With the exponential increase in computing power over the last 30 years, research groups rely heavily on the results of simulation for design and decision making processes. In order to ensure that the solutions provided by these simulations are sufficiently accurate, it is necessary that the models be validated to determine their uncertainty. The U.S. Department of Defense (DoD) released a recommended practices guide for the Verification, Validation and Accreditation (VV&A) of Models and Simulations (M&S) [2] for more informed judgment and assessment. In 1998 the American Institute for Aeronautics and Astronautics (AIAA) published a standard to be used for the verification and validation of CFD models [3]. The American Society of Mechanical Engineers (ASME) also published a standard for Verification and Validation (V&V) of CFD and heat transfer in 2009 called V&V-20 which has been extended from the AIAA standard to include heat transfer problems [4]. Verification and validation is a critical part of model development and application in simulation use.

Using these standards, one can ensure that the simulation results are accurate. According to Oberkampf and Roy [5], "Validation is the process of assessing the physical accuracy of a mathematical model based on comparisons between computational results and experimental data." In contrast to discovery experiments where the experimentalist is attempting to discover or understand more about a certain physical phenomenon, *validation experiments simply look to measure the physical nature of a system for the purpose of providing a complete description of the system which can be used to test the validity of a model* [6].

Validation of complete, large-scale systems is generally not feasible to perform. Methodology for a hierarchical approach to validation has been outlined in [7–10]. Figure 1 shows the validation hierarchy

for complete systems which are broken down into smaller subsystems for validation purposes. According to this hierarchy, the present work is considered a Benchmark-Level case due to the highly coupled fluid flow and heat transfer occurring in the flow domain.

When performing a validation experiment, careful documentation of all *boundary conditions* (BCs), *initial conditions* (ICs) and *system response quantities* (SRQs) and their associated uncertainties is vital. Examples of boundary conditions may be locations of physical walls/geometries or the temperature distribution of a surface. Initial conditions are similar to boundary conditions but exist at the start of an experiment and change over time, for example, the temperature response of a body after starting an electric heater. System response quantities are the outputs of the system that are recorded for comparison to the output of a simulation such as a velocity profile in the fluid domain or wall shear field at a boundary. System response quantities are provided to the analyst *after* performing the simulations in order to ensure that the data are used for validation rather than model calibration [5].

Careful experimental design is needed in order to have sufficient insight to plan for SRQs to be measured. Modelers and experimentalists should be involved through all aspects of the design and execution of a validation experiment for optimum success. Knowledge of the relative difficulty of specific SRQs will aid both parties in exercising the limits of the CFD model especially in cases of complex physics. Figure 2 shows the spectrum of SRQs and their relative difficulty to both measure and predict. Using this spectrum in the planning stages of a validation study allows for more rigorous testing of the models applied.

Uncertainty quantification is the process used to assess the applicability or credibility of a CFD model as part of validation. A validation metric is a difference operator used to compare the computational and experimental results. From the ASME V&V-20 Standard [4], the validation comparison error E is defined as the difference between the simulation solution S and the experimental data D as

$$E = S - D. \tag{1}$$

Assuming that the error sources are independent, the validation uncertainty is the estimate of the numer-

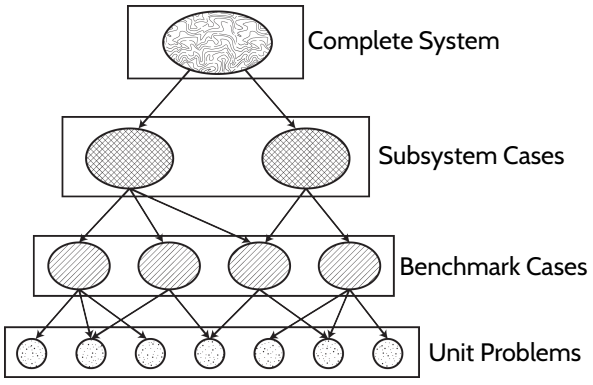

Fig. 1. The validation hierarchy and their descriptions as presented in [3].

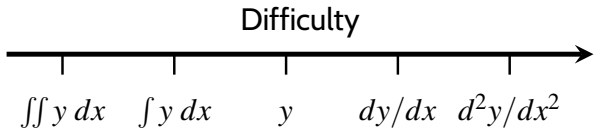

Fig. 2. Spectrum of difficulty to measure or acquire an arbitrary SRQ, $y(x)$, after [5].

ical uncertainty and experimental uncertainty and, for measured variables, is calculated by

$$U_{\text{val}} = \sqrt{U_{\text{num}}^2 + U_{\text{input}}^2 + U_D^2} \tag{2}$$

where U_{num} is the numerical uncertainty of the model, U_{input} is the simulation uncertainty due to errors in the boundary conditions and U_D is the experimental SRQ uncertainty. The validation comparison error is satisfactory if the validation comparison error E is sufficiently smaller than the validation uncertainty U_{val} for the intended application of the model. This work will provide U_D for the SRQs used to validate the CFD models as well as uncertainties of the BCs applied to the CFD models in order to determine U_{input}.

Oberkampf and Roy [5] describe a generalized validation metric using multiple experimental results in which the estimated error in the model is described by

$$\tilde{E} = y_{\text{m}} - \bar{y}_{\text{e}} \tag{3}$$

where y_{m} is the SRQ from the model and $\bar{y}_{\text{e}}$ is the estimated mean based on n experiments conducted and is given by

$$\bar{y}_{\text{e}} = \frac{1}{n}\sum_{i=1}^{n} y_{\text{e}}^{i}. \tag{4}$$

It can then be shown that the true error in the model has the bounds of

$$y_{\text{m}} - \bar{y}_e - t_{\alpha/2,v} \cdot \frac{s}{\sqrt{n}} < E < y_{\text{m}} - \bar{y}_e + t_{\alpha/2,v} \cdot \frac{s}{\sqrt{n}} \tag{5}$$

where $t_{\alpha/2,v}$ is the quantile of the t distribution for $v = n-1$ degrees of freedom and s is the sample standard deviation. Using this validation metric allows for inclusion of multiple validation experiments in determining the comparison error, decreasing the interval by $1/\sqrt{n}$ as more experimental data is included.

1.2 Natural Convection

Heat transfer from fluid motion due to density gradients resulting from a heated object is known as free or natural convection. Convection heat transfer is characterized by the heat transfer coefficient h which comes from Newton's Law of cooling

$$q = hA_s(T_s - T_\infty) \tag{6}$$

where the heat transfer q to or from the object is equal to the product of h, the surface area A_s and the temperature difference between the surface T_s and the surrounding fluid T_∞. The Rayleigh number, Ra$= g\beta(T_s - T_\infty)L^3/(\nu\alpha)$, is useful for determining transition to turbulence which, for a vertical heated plate, is generally assumed to occur at Ra $\approx 10^9$. Here, g is the acceleration due to gravity, β is the coefficient of thermal expansion, L is the distance along the flat plate, ν is the kinematic viscosity and α is the thermal diffusivity.

In general, the heat transfer coefficient is unknown. The convection coefficient depends on flow conditions and is generally low for free convection and much higher for forced convection. This coefficient is also larger for liquid flows compared to gaseous flows and can be very large for boiling. Also, the convection coefficient is generally lower for laminar flow regimes than turbulent regimes due to increased boundary layer mixing of near-wall fluid. In most cases, correlations based upon large sets of experimental data are used to determine the dimensionless heat transfer coefficient or Nusselt number

$$\mathrm{Nu} = \frac{h\,L}{k_f} \tag{7}$$

where k_f is the thermal conductivity of the fluid. For natural convection, these correlations are a function of Rayleigh number and Prandtl number ($\mathrm{Pr} = \nu/\alpha$). The convection coefficient can be determined by using these empirical correlations. In many cases when the flow conditions cannot easily be determined due to complex geometry, the only practical approach is to determine the Nusselt number experimentally [11].

Few validation studies exist for buoyantly driven flows. De Vahl Davis [12] and De Vahl Davis and Jones [12] were among the first to perform benchmark studies for natural convection in an enclosure, although these benchmarks were using CFD simulations on uniform meshes of up to only 81×81 cells due to limited computational resources at the time and were compared to analytical solutions for the laminar flow regime.

The first full validation experiment of this type was performed in 1998 by Leong, *et al.* [13] for natural convection in a cubical cavity with opposing faces at different temperatures. The authors report Nusselt numbers accurate to 1% for Rayleigh numbers in the laminar flow regime. The experimental results were compared to CFD for $\mathrm{Ra} = 4 \times 10^4$ and found to be accurate to within 0.3%. Later, Leong, *et al.* [14] also performed benchmark experiments using the same apparatus for a wider range of Rayleigh numbers up to 10^8 in order to determine Nusselt numbers for the cavity at different tilt angles.

Other variations of validation experiments for natural convection in cavities were later performed. Mamun, *et al.* [15] provide an extension of Leong's previous publications by using a "double inclined" cubical cavity for Rayleigh numbers ranging from 10^3 to 3×10^8. Ampofo and Karayiannis [16] performed validation experiments for turbulent natural convection in a square cavity ($\mathrm{Ra} > 10^9$).

Betts and Bokhari [17] have provided a detailed validation study for turbulent natural convection in an enclosed tall cavity. This study not only provides integral quantities such as the Nusselt number and heat transfer coefficient but also temperature and velocity profiles through the vertical direction of the experiment. The experiment presented is very extensive and provides substantial detail for use in CFD validation. Tian and Karayiannis [18] also performed a turbulent benchmark experiment for a square cavity providing both velocity and temperature profiles within the cavity for use in validation. These two studies have provided high-quality validation data for natural convection flows. However, they are only applicable to recirculating cavity flow. Natural convection open channel flow can be a much more difficult problem to simulate due to tight coupling of fluid flow with fluid properties where slight variations in boundary conditions can dramatically affect the solution.

Natural convection flows differ from forced convection flows by their BCs. Forced convection is driven by an inflow BC or applied pressure gradient. For natural convection, however, a temperature or heat input BC induces flow due to the temperature gradient and effects of buoyancy. Thus, application of an inflow BC to natural convection over-prescribes the solution, allowing the inflow measurement in natural convection problems to be used as an SRQ.

1.3 Turbulence Models

This work involves the modeling of a low Mach number gas flowing upward along the outside of vertical heated cylinders within an overall. The relevant Grashof numbers exceed 10^9 so that the boundary layers are expected to be turbulent. In addition, the heating rate may be sufficiently high such that the fluid properties vary significantly along the cylinder in both the radial and axial directions. Consequently, the flow is continually adjusting to the varying fluid properties.

Several studies aimed at the discovery of physics of flow along arrays of vertical cylinders are available. Most recently, Rafique et al. [19] presented laminar results for flow along four different vertical cylinder geometries. This most relevant study to the present work involved an open rectangular pitch assembly of cylinders intended to model fuel rods in a spent fuel bay. A constant heat flux of 22.2 W/m^2 was employed on the cylinder walls. However, citing long computational times, and following Davis and Perona [20], they simplified the problem in a manner that permitted a two-dimensional approximation. Their results showed maximum axial velocities on the order of 0.4 m/s. Krishna et al. [21] performed a combined numerical and experimental investigation of natural convection in a partially heat generating 19-rod bundle inside an enclosure. Heating rates were sufficiently low that flow regimes were laminar (Ra $\leq 10^9$), and the numerical model approximated the rod bundle as a porous medium to reduce complexity. Temperature distributions within the tube bundle were reported to have been predicted satisfactorily. McCann [22] also developed a computer code based on a porous media formulation to treat rod-bundle configurations. Other relevant studies have been carried out by Davis and Perona [20], Koenig and Buchanan [23], and Driesen et al. [24]. In the present work, the buoyancy-driven flow over an array of heated vertical cylinders is investigated numerically. The numerical solutions are compared with experimental data available for this configuration as discusse in Section 2. The experimental results indicate that the Grashof number is greater than 10^9. Consequently, for modeling purposes, the flow was considered turbulent.

2 Validation Benchmark Data Study

2.1 Experimental Facility

The Rotatable Buoyancy Tunnel (RoBuT) is a rotatable wind tunnel facility at Utah State University designed for performing CFD validation benchmark experiments with buoyancy either aiding or opposing the flow, depending on the tunnel orientation. The wind tunnel is shown in Fig. 3 with the major components labeled. The facility test section is a square cross-section of 0.305 m $\times$ 0.305 m and is 2 m in length. The coordinate system lies at the center leading edge of the opaque wall as shown with the positive z-axis being aligned with the stream-wise direction.

The fluid enters through the bottom of the inlet contraction and flows upward. Flow entering the wind tunnel first passes through an array of 1/4 in., Schedule 40 PVC tubes with $\varnothing$ 3.2 mm holes spaced 25.4 mm apart through which olive oil vapor is introduced into the flow. It then passes though a single row, aluminum fin/copper tube heat exchanger (which was unused for these benchmark experiments but still present in the flow) followed by a honeycomb flow straightener and finally two high porosity screens. The fluid then accelerated uniformly through the inlet contraction which had an area ratio of 6.25:1 and was 0.914 m in length before entering the test section. The flow conditioning system was not modeled due to its high complexity. Instead, the pressure drop was measured and should be used as a boundary condition.

The test section is constructed of three transparent polycarbonate walls with several anti-reflective windows for optical access during fluid measurement and an opaque aluminum wall for structural rigidity. The construction of the test section and fuel rod bundle will be discussed in Section 2.2.

After leaving the test section, the fluid passes through the outlet transformation which is constructed of four sections that are bolted together. The transformation converts the 0.305 m $\times$ 0.305 m test section

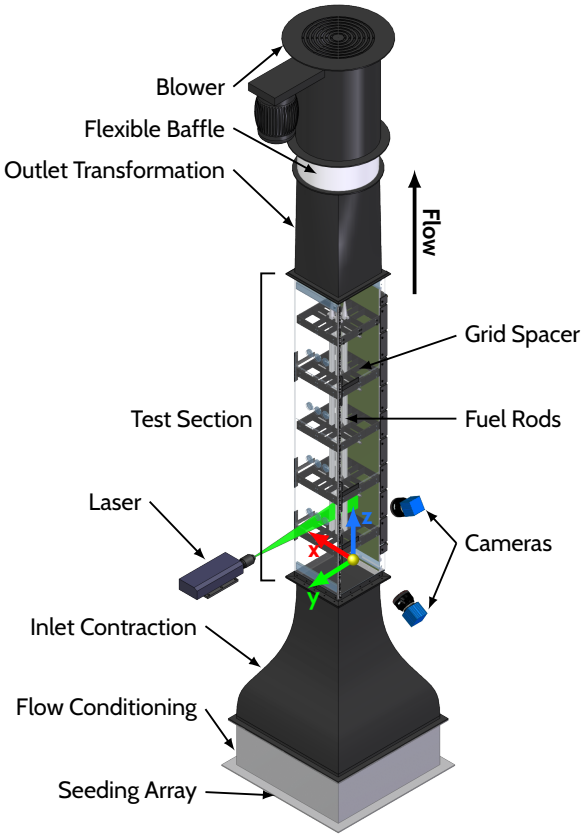

Fig. 3. A schematic of the wind tunnel showing the major components used in this study.

cross-section to a circular cross-section of ∅ 102 mm over a length of 0.686 m. A flexible baffle between the outlet extension and blower was removed in order for the fluid to freely exit the test section.

The inlet contraction and outlet extension are constructed of fiberglass with a highly polished gel coating. The outlet extension is formed from four sections while the inlet contraction is a single piece.

Two Laskin nozzle seeding canisters were used to introduce seed to the fluid flow for PIV measurements. The particle diameter of the olive oil vapor produced by the seeders is a function of line pressure and nozzle hole diameter [25]. A TSI Aerodynamic Particle Size Spectrometer was used to measure the physical particle diameter and was found to have a mean of 1.7 µm. Air was pumped through the body of the seeding canisters in order to dilute the seed exiting the PVC array before being entrained. Holes of ∅ 3.2 mm were used to evenly disperse the seed into the flow. The volume fraction of the seed was found to be $\sim 10^{-9}$, having little effect on the thermodynamic properties of the air and can reasonably be neglected.

2.2 Test Section and Fuel Model

The test section has a 0.305 m × 0.305 m (12 in. × 12 in.) internal cross-section and is 2 m in length. Three of the four walls are constructed of transparent Lexan™ polycarbonate and are 12.7 mm thick. The fourth wall is constructed of a 12.7-mm thick Aluminum 6061-T6 plate for structural rigidity and has been painted flat black and coated with a rhodamine fluorescent die for filtering reflections during PIV data acquisition. Each wall is divided into four interlocking sections for ease of manufacturing, assembly and maintenance. The top wall panels (opposite the aluminum wall) are easily removed for internal cleaning as well as for PIV calibration throughout the duration of the experiment. Rectangular optical windows are placed at the inlet of the test section for PIV measurements to reduce the amount of refraction inside the polycarbonate walls. Circular optical windows are placed at the midpoint in the

z-direction between each grid spacer for PIV measurements in the flow-wise direction.

The coordinate system used in this study is shown in Fig. 3. The coordinate system is located at the center of the leading edge of the opaque, aluminum wall. The left and right walls are positioned at $x = 152.4$ mm and $x = -152.4$ mm, respectively, while the top wall is position at $y = 304.8$ mm.

The fuel model consisted of four 1.58-m-long 6061-T6 aluminum cylinders of ∅ 31.75 mm, each divded into four interlocking sections, referred to herein as rod sections. Contained in each rod section is a 20 W split-sheath cartridge heater from Dalton Electric (Part No. W3H126) of ∅ 9.53 mm and 323.85 mm in length with a 314 mm heated length. The heaters were powered by two BK Precision Model 9174 programmable power supplies. A constant power condition was applied to the heaters in order to achieve a desired rod surface heat flux. Each rod section was constructed of two pieces machined internally to house the cartridge heaters and thermocouples (TCs). The TCs were embedded inside the rods with thermally conductive epoxy (Dow-Corning 3-6751) and routed outside the rods and test section via an aluminum-wire conduit. Two cylinder halves were bolted together using six #8-32 stainless steel screws with 2.3 N-m torque. The counter bore holes were filled with 6061-T6 aluminum rod using Duralco 4540 machinable epoxy.

Oxidation of aluminum causes wide variation in radiative properties [26, 27]. The outer surface of the rod sections was plated with electroless nickel to generate low, constant emissivity for reduction of radiation heat transfer. The total hemispherical emissivity of the plating was measured by Optotherm Thermal Imaging and reported as $\varepsilon_s = 0.10 \pm 0.01$. Any unplated surfaces of the fuel rod assembly were polished. Figures 4 and 5 show the surfaces of the model that were plated and polished. Ceramic spacers were placed between the rod sections and wire conduit to eliminate conductive heat transfer.

A hemispherical aluminum cap was placed on the upstream end of each fuel rod to limit flow separation which results in long time-scale turbulent fluctuations. Similarly, the trailing end of each fuel rod was treated with 128-mm-long aluminum cones to maintain attached flow. Fiberglass tape was used to thermally isolate the cones from the heated rods. Aluminum bars were attached to the trailing end of the rods for suspending the fuel rods in the test section.

Steel 4130 grid spacers, designed similar to corrugated box separators, were used to maintain fuel rod spacing in the assembly. Aluminum borders were machined with slots to maintain the grid spacer shape and were embedded in the polycarbonate walls such that the interior walls of the test section were smooth as shown in Fig. 6. The rods were centered in the grid spacers with fiberglass-tipped, #4-40 set screws. Swirl elements were designed as a simple $45° - 45° - 90°$ triangle bent at $45°$ from vertical towards the rods as shown in Fig. 9. The swirl elements were placed in the first four grid spaces in the stream-wise direction while the final grid spacer did not have swirl elements in order to accommodate the aluminum bars used to suspend the fuel rods in the test section. Two swirl elements are bent towards each rod resulting in a 17.9% blockage ratio. While considerably less effective at

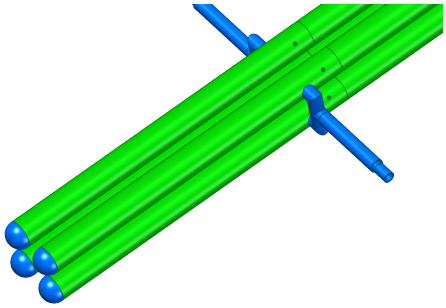

Fig. 4. Surface treatment of the leading edge of the fuel rod assembly. Blue surfaces represent polished aluminum and green surfaces represent nickel plating.

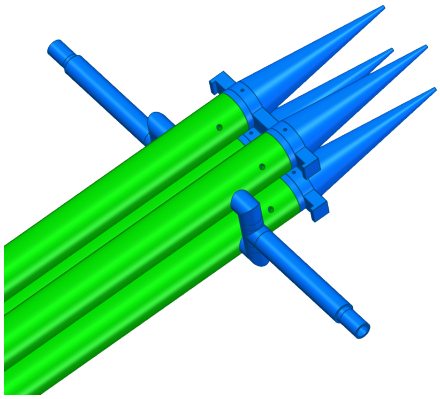

Fig. 5. Surface treatment of the trailing edge of the fuel rod assembly. Blue surfaces represent polished aluminum and green surfaces represent nickel plating.

mixing than commercially produced mixing vanes, this shape still generates the same physics that are present in an actual fuel bundle.

The pitch-to-diameter ratio of the assembly is 1.52. The rod diameter and pitch-to-diameter ratio are larger than a prototypical PWR assembly which was necessary to allow for instrumentation and assembly purposes but still allows the model to capture the physics associated with dry fuel storage.

2.3 Instrumentation and Facility Control

Various TCs were placed in the facility for controlling and monitoring room conditions. TCs and a proportional-integral-derivative (PID) controller used the heating and air conditioning system to maintain a room temperature at $20^{\circ}\text{C} \pm 1.0^{\circ}\text{C}$ through the duration of the study. The ambient temperature and relative humidity were measured using an Omega HX93A relative humidity and temperature sensor with measurement uncertainties of $\pm 2.5\%$ for humidity and $\pm 0.6^{\circ}\text{C}$ for temperature. Ambient pressure was recorded using an SB-100 barometric pressure sensor from Apogee Instruments with a measurement uncertainty of $\pm 1.5\%$. An NI USB-9215A 4-channel, ± 10 V, 16-bit, Analog Input DAQ was used to measure the voltage from each of these sensors. Samples at 1 Hz were acquired then averaged and

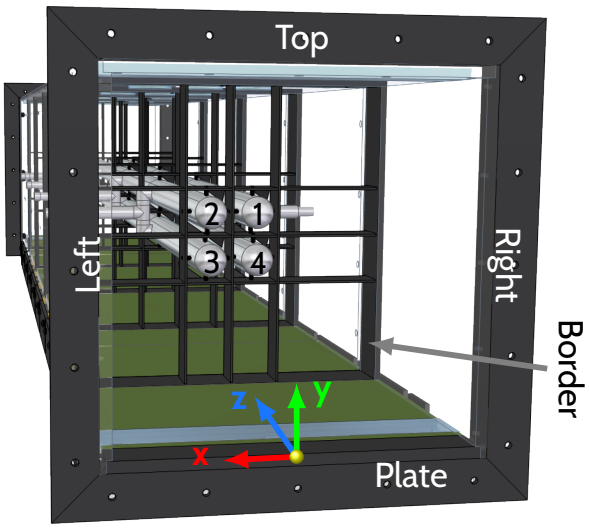

Fig. 6. Inlet view of the test section with several important features labeled. The 'Border' is the frame used to maintain grid spacer shape. It is embedded in the test section walls such that the walls themselves are smooth.

recorded once per minute. The ambient temperature, atmospheric pressure and relative humidity are sufficient to determine air properties. It should be noted that the atmospheric pressure is much lower than one standard atmosphere due to the elevation where the data were acquired (1456 m above sea level). The air properties are included in the AmbientConditions.csv files for the respective cases.

Fifteen TCs (in a 5×3 array in the x and y directions, respectively) were placed immediately downstream of the honeycomb flow straightener at the inlet of the wind tunnel (on the $z = -0.941$ m plane) for measuring the incoming fluid temperature. The temperature distribution at wind tunnel inlet and test section inlet were assumed to be the same when calculating mass flow rate through the wind tunnel. The inflow temperatures are found in the InflowTemperatures.csv files.

It is not feasible to model the complex geometries found in the flow conditioning portion of the wind tunnel. Therefore, the pressure drop across this portion of the wind tunnel was measured using a 1-Torr Baratron-differential-pressure sensor connected to a MKS207D Singal Conditioner. The voltage output by the signal conditioner was read using an NI-9205 16-channel, $\pm$ 10 V, 16-bit, Analog Input module. A total of 3000 samples were acquired at 5 Hz and averaged for each test case. The pressure drop for each case are available in the FlowConditionerPressureDrop.csv files.

Preliminary CFD simulations were performed during the design phase of the experiments and found no wall temperature variation across the lateral direction of each wall though there were slight temperature gradients in the stream-wise direction. Thus, 21 TCs were placed within 2.5 mm of the inner surface of each wall at 3 evenly-spaced lateral positions and 7 stream-wise positions, near the inlet, slightly downstream of each grid spacer and near the outlet.

As mentioned previously, TCs were embedded inside each rod section. Preliminary CFD simulations also indicated variation in surface temperature due to the presence of the swirl elements near the rods. It was determined that four TCs would be placed circumferentially at three stream-wise positions in each rod section for a total of 48 TCs per fuel rod. Machining of the internals of each rod section allowed the TCs to be placed at 2.5 mm of the rod surface. TCs were aligned with the small gap between adjacent fuel rods and at 90° spacing at a given stream-wise position.

All four heaters in the rod sections at a given stream-wise position were wired in parallel and powered from a single output from the power supply. Measurement of the un-powered heater resistance indicated a variation of 178.1 ± 0.98 Ω and the current was assumed to be evenly distributed to each heater. The current supplied to the heaters was read from the programmable power supplies which had a readout uncertainty of $\pm 0.1\%$ and bias uncertainty of 1 mA. The voltage across the four heaters at each stream-wise position was measured using a voltage divider circuit and an M-series NI PCI-6221 DAQ card. High accuracy, ultra-stable film resistors from Caddock of 10 MΩ and 1 MΩ (Part No. USF240-10.0M-0.1%-2PPM and USF240-1.00M-0.1%-2PPM, respectively) made up the voltage divider circuit each with an accuracy of $\pm$ 0.1%.

Sixteen TCs (in a 4×4 array) placed at the outlet of the test section ($z = 2$ m) in an evenly-spaced square grid pattern. TCs were suspended by four ∅ 1.58 mm steel rods and routed outside the test section through the aluminum wall. The TCs were evenly spaced 61 mm apart in both the x- and y-directions and the array was centered in the test section outlet.

The TCs placed inside each rod section, inside the polycarbonate walls, and at the test section outlet were welded in-house using an Argon-shielded welder. Fiber-glass shielded Type-K TC wire from Omega with Special Limits of Error was used. Each of these TCs were calibrated using an Isotech FASTCAL-M calibrator with an accuracy of 0.3°C across a range of $30 - 180$°C. An average calibration curve was applied to these TCs because they were made from the same spool of wire. Outside this range, an uncertainty of 1.1°C from the manufacturer was used. All other TCs in the facility (including the inlet TCs described previously) were uncalibrated and the manufacturer's uncertainty of 1.1°C was used. The cold-junction compensation of the NI-9213 modules had an accuracy of 0.8°C applied to the uncalibrated TCs.

2.3.1 Particle Image Velocimetry

All fluid velocity measurements were made using a stereoscopic PIV system that provides non-intrusive velocity field measurements. Two Imager sCMOS cameras from LaVision [28] were employed with a dual cavity Quantel Evergreen (frequency-doubled 532 nm Nd:YAG, 100mJ/pulse, 25 Hz per cavity) and a programmable timing unit. Focusing optics and a cylindrical lens were placed on the front of the laser to convert the laser beam to a sheet with adjustable thickness. The Imager sCMOS cameras had a 16-bit CMOS sensor that was 2560 $\times$ 2160 pixels with a pixel size of 6.5 µm with acquisition speeds of up to 50 frames per second.

The cameras were fitted with Nikon AF Nikkor 28 mm f/2.8 D fixed focal length lenses for inlet velocity measurements. Scheimpflug mounts were used to align the focal plane of camera and lens such that the entire field of view is in focus. These add approximately 12 mm to the lens focal length. The configuration used for acquisition of the inlet velocity profile is shown in Fig. 7. The lenses were changed to Tamron Telephoto AF 180 mm f/3.5 Di Macro fixed focal length lenses, while still using the Scheimpflug mounts, for all SRQ data locations. The cameras were placed at approximately 15° half angle vertically at each SRQ location as shown in Fig. 8.

Optical rails from were used for camera adjustment in the flow-wise direction. Three linear traverses were used for positioning the cameras in the xy-plane and for adjusting the laser position in the x-direction. The repeatability of the traverses was 0.005 mm. After positioning the cameras and laser, DaVis version 8.3.0 software [29] by LaVision controlled image acquisition, processing and vector calculation, including uncertainty. All PIV measurements made for this study are stereoscopic resulting in 3-components of velocity in the laser plane with uncertainty.

PIV calibration for inflow measurements was performed by mounting a two-plane calibration plate inside the wind tunnel at the inlet plane ($z = 0.067$ m). The 11.875 in. square, two-plane calibration plate consists of holes of 0.125 in. diameter are evenly spaced every 0.625 in. and the distance between planes is 0.125 in. The plate was mounted directly to the test section and the laser was then aligned with the plate. The calibration images were dewarped using a 2-dimensional third order polynomial fit. The laser sheet for the inflow measurements was approximately 4 mm thick.

A much smaller, single plane calibration plate was used for the SRQ measurement calibration. A two-dimensional dot array Max Levy Autograph calibration plate was traversed through the laser sheet thickness for multiple plane calibration. The calibration plate consisted of ∅ 0.25 mm dots spaced 0.5 mm apart and was 50 mm $\times$ 50 mm in size with a replication error of less than 0.001 mm. The calibration plate was mounted to a Velmex traverse and images of the target were acquired at -1 mm, 0 mm and 1 mm within the laser sheet, where 0 mm corresponds to the center of the sheet and the sheet

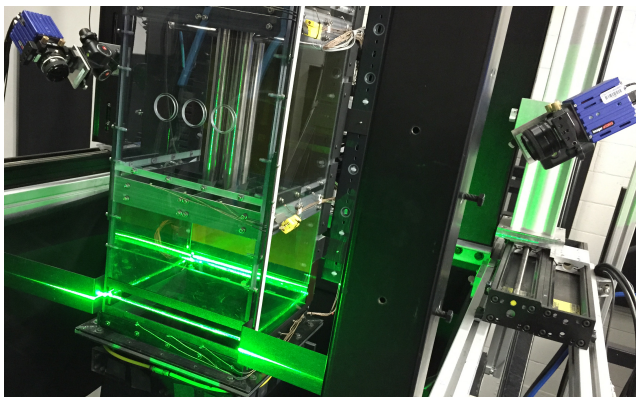

Fig. 7. A photograph of the PIV setup used to acquire inlet velocity profiles. The laser is fired in a horizontal sheet from the bottom left corner of the image.

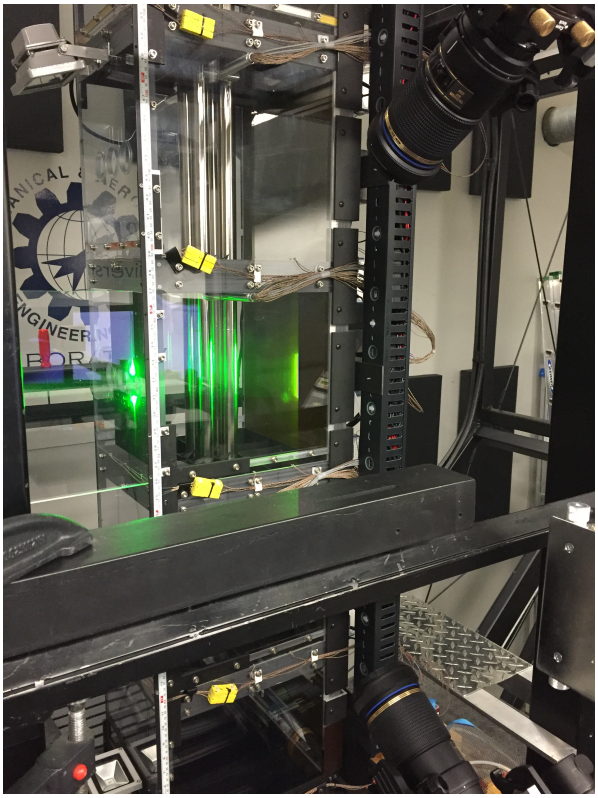

Fig. 8. A photograph of the PIV setup used to acquire SRQ velocity measurements. The camera lenses are shown in the upper right and lower right corners with the cameras out of frame. The laser is fired in a vertical sheet from the left of the image.

was 2 mm thick. Every other dot on the calibration target was used for calibration to limit processing time need for the dot locating algorithm. The same third-order polynomial fit was used for the SRQ calibration as the inflow calibration. Due to geometric constraints, it was not possible to calibrate inside the test section. Therefore, a sheet of clear polycarbonate was mounted to the exterior of the test section inline with the test section wall during calibration to account for refraction issues caused by wide-angle placement of the cameras.

Prior to acquisition, the lens aperture, laser intensity, and seeding density were adjusted to produce optimal particle image quality and particle density. The time between images, dt was then adjusted such that the displacement was between 4-16 pixels to achieve optimal displacement and limit the number of particles leaving the laser plane between images. Particle image diameter and density were determined based on the method presented in [30].

Images were processed using multi-pass, window-deformation in DaVis. A geometric mask was applied to the images to eliminate the influence of walls/rods on the correlation after which the average of the dataset was subtracted from the images to remove background information. Two passes of the cross-correlation were completed with 64 $\times$ 64 square interrogations windows followed by four passes of 32 $\times$ 32 round interrogations windows with flow-based window deformation and symmetric displacement. Each pass was completed with 75% window overlap. Vector post-processing was then performed to remove vectors with a peak ratio less than 2. Vectors were 'strongly removed & iteratively replaced' by a two-pass median filter to correct spurious vectors if the value was larger than one standard deviation of its neighbors. Vector field statistics were then calculated, with uncertainty, for the dataset including mean and standard deviation vector fields, Reynolds stresses, turbulence kinetic energy and turbulent shear stress.

2.3.2 Uncertainty Quantification

Uncertainties in this work were quantified using the methods presented in Coleman and Steele [31]. The total uncertainty of a measured quantity r is a function of the bias B and random uncertainty S

$$U_r = \sqrt{B_r^2 + S_r^2} \tag{8}$$

where B_r is the root-sum-square of all bias sources for the instrument. Uncertainties presented in the data provided with this paper are at 95% confidence.

Uncertainty for velocity measurements were calculated using the Direct Image Correlation [32] method built into the DaVis software. According to Wieneke and Sciacchitano [33], the uncertainty of a single mean velocity vector is calculated, assuming a large sample size, using

$$U_{\bar{x}} = \frac{\sigma_x}{\sqrt{N}} \tag{9}$$

where σ_x is the standard deviation of the velocity vectors at a single location for the dataset and N is the number of vectors at each location. This method assumes that the samples are statistically independent and follow a normal distribution.

2.3.3 Fluid Properties

All fluid properties used in this study were calculated using the fluid temperature, atmospheric pressure and relative humidity measurements described in Sec. 2.3. The fluid specific heat was estimated using the third-order polynomial fit presented in Volume 6 of Thermophysical Properties of Matter [34]. The fluid thermal conductivity was estimated using a linear interpolation of tabulated data presented in Volume 3 of Thermophysical Properties of Matter [34]. The remaining properties were calculated using standard psychrometric relationships and are presented in Appendix C of [1].

2.4 Data Acquisition

The BCs and SRQs presented for these benchmark experiments are presented in Table 1. All of the SRQs presented in this study are directly measured quantities, with exception of the mass flow rate which is a double integral, on the difficulty spectrum in Fig. 2.

Temperatures were acquired at steady-state at two heat flux cases, 400 W/m^2 and 700 W/m^2. Each SRQ velocity dataset consisted of 1000 images acquired at 0.1 Hz in order to have statistically independent samples. The inflow velocity fields consisted of 1000 images acquired at 2 Hz. The laser sheet was 2-mm-thick for the SRQ velocity measurements and 4-mm-thick for the inflow measurements. The laser sheet for inflow measurement was aligned with the stream-wise velocity component traveling through the thickness of the laser sheet. This required a larger thickness than usual in order to have sufficient particle displacement between camera frames for low measurement noise. The 2-mm-thickness of the laser sheet for SRQ meausrements was required for sufficient particle displacement in the x-direction for the PIV system while the width of the laser sheet was aligned with the stream-wise component as shown in Figs. 3 and 8.

Prior to acquiring the final sets of data at each location, preliminary data were acquired at 1 Hz and processed to check for sample independence. An autocorrelation was applied to the fluctuating stream-wise velocity component w' and integrated from zero lag to the time of the zero-crossing after [33]. For 1000 images, the effective number of samples was 100, indicating the need to acquire images 10 times slower. Sample data were then acquired at 0.1 Hz and an autocorrelation was applied in the same manner. The resulting autocorrelation indicated statistical independence.

Table 1. A list of the boundary conditions and system response quantities available for download with this study.

BCs	SRQs
Geometry	Wall Temperatures
Atmospheric Conditions	Rod Temperatures
Rod Heater Power	Inlet Velocity
Inlet Pressure Drop	Downstream Velocity Profiles
Inlet Temperature	Outlet Fluid Temperature
Rod Surface Emissivity	Mass Flow Rate

2.4.1 Inlet Velocity Measurement

The test section inlet velocity data were acquired at the $z = 67$ mm plane. The laser sheet was oriented parallel to the xy-plane such that the stream-wise velocity component was aligned through the laser thickness. Inlet velocity fields and centerline profiles are shown in Figs. 17-20. The inflow velocity field was integrated to determine volume flow rate through the wind tunnel. Inflow mean velocity field measurements are found in InletVelocityField.csv and inflow Reynolds stresses and turbulence kinetic energy fields are found in InletReynoldsStressField.csv with turbulence kinetic energy indicated as 'TKE' and Reynolds stresses as 'RS' followed by the two directions of the stress, i.e. 'RSXY' is the Reynolds shear stress in the xy-direction or $\overline{u'v'}$.

Using the volume flow rate and the measured pressure drop across the inlet flow conditioning, the loss coefficient across the flow conditioning system is determined and shown in Table 2. The loss coefficient was calculated by

$$K = \frac{2\,\rho\,A^2\,\Delta P}{\dot{m}^2} \tag{10}$$

where the fluid density ρ and the mass flow rate $\dot{m} = \rho Q$ were calculated using standard psychrometric relationships for humid air. The density was determined using the mean inflow temperature of the 5×3 array of inlet TCs and the ambient pressure and relative humidity measured in the facility. The volume flow rate Q through the inlet was calculated by integrating the w-velocity component of the test section inflow measurement. The calculated mass flow rate through the test section is found in MassFlowRate.csv. Inflow temperature measurements of the inlet TC array are found in InflowTemperatures.csv.

Table 2. Volume flow rate Q, pressure drop ΔP and loss coefficient K across the inlet flow conditioning for each test case in order of increasing volume flow rate.

Case Name	Q, [m^3/s] $\pm$	ΔP, [Pa] $\pm$	K $\pm$
Natural400	0.019±0.0016	0.123±0.022	233±56
Natural700	0.024±0.0021	0.153±0.021	166±35

It should be noted that the inflow velocity profile is not a BC but an SRQ for natural convection. The flow is driven by the effects of buoyancy due to the temperature gradient generated by the heated rods and not by an imposed velocity at the inlet as would be present for forced convection. The integral of the inlet velocity field, however, was used to determine the mass flow rate through the wind tunnel in order to determine the loss coefficient across the flow conditioner. A velocity profile is a more rigorous validation metric than the double integral of velocity (see Fig. 2) used to determine the loss coefficient. The user of these data should be aware that using the pressure drop is a more accurate representation of the flow conditioner and the loss coefficient should be used with caution.

2.4.2 SRQ Velocity Measurement

Velocity measurements were made on the $x = 0$ m and $x = -0.06$ m planes at $z = 0.476$ m, 0.825 m, 1.174 m and 1.524 m. The locations of the velocity profiles presented for validation in this study are shown in Figs. 9 and 10.

2.5 Boundary Conditions

Each fuel rod containes four cartridge heaters. The spacing between these heaters needed for routing of the wiring outside the test section resulted in a piece-wise heating boundary condition on the inner surface of the fuel rods. Table 3 shows the heating locations for each rod section in the z-direction and the power applied to all four rod sections at the respective z-position for both heating conditions. The power listed is the power supplied to all four cartridge heaters at the given z-position and is assumed to be divided between them evenly.

The fluid temperature entering the wind tunnel was measured using the inlet TC array described in Sec. 2.3 which were positioned on the $z = -0.941$ m plane. The pressure drop present upstream of the contraction inlet due to the presence of the flow conditioner and seeding array is presented in Table 2.

The walls of the test section were heated slightly due to the growth of the boundary upon reaching steady-state and by radiation heat transfer. The amount of heat lost through the walls due to heating was calculated using the mean wall temperature and the standard Nusselt number correlation for a vertical

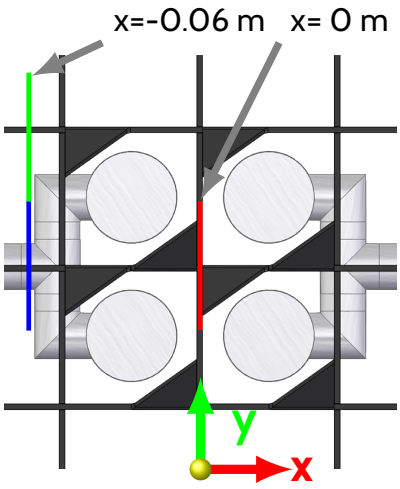

Fig. 9. Locations in the xy-directions of the PIV field of views for SRQ data acquisition. The coordinate system is shown for directional reference only and does not correspond to the actual location of the origin. The blue and green windows are centered at $y = 0.152$ m and $y = 0.197$ m, respectively. The red field of view is centered at $y = 0.152$ m on the $x = 0$ plane.

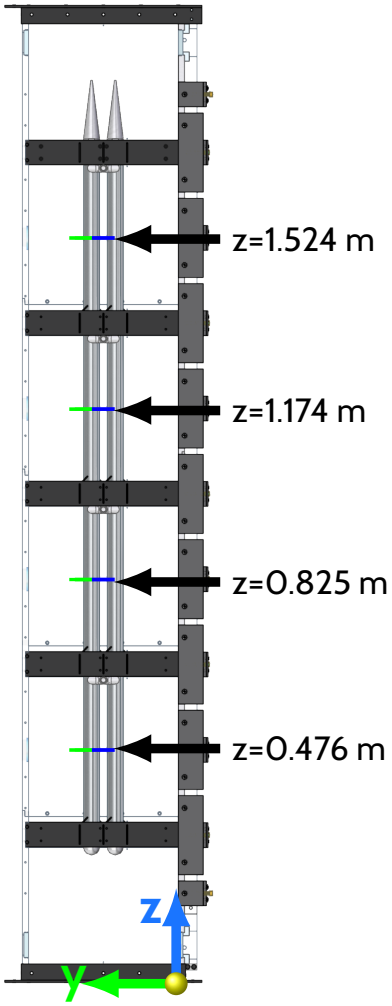

Fig. 10. Locations in the yz-plane of the PIV viewing windows for SRQ data acquisition. The blue and green windows are centered at $y = 0.152$ m and $y = 0.197$ m, respectively, on the $x = -0.06$ m plane. The fields of view on the $x = 0$ m plane are aligned in the y and z directions with the blue fields of view.

Table 3. Heating BCs for the fuel rods for both heat flux cases. Power was applied to the internal surface of the fuel rods over the ranges specified and is applied to all four rod sections at a given z-position.

z-Position Range, [m]	Natural400 Case Power Input, [W]	Natural700 Case Power Input, [W]
$0.279 - 0.593$	56.23 ± 0.13	98.99 ± 0.21
$0.593 - 0.627$	Unheated	Unheated
$0.627 - 0.941$	56.92 ± 0.13	98.61 ± 0.21
$0.941 - 0.976$	Unheated	Unheated
$0.976 - 1.290$	56.77 ± 0.13	98.32 ± 0.21
$1.290 - 1.325$	Unheated	Unheated
$1.325 - 1.639$	56.95 ± 0.13	98.61 ± 0.21

flat plate from [35]

$$\overline{\mathrm{Nu}}_L = \left\{ 0.825 + \frac{0.387\mathrm{Ra}_L^{1/6}}{\left[1 + (0.492/\mathrm{Pr})^{9/16}\right]^{8/27}} \right\}^2 . \tag{11}$$

The heat lost through the polycarbonate walls for both cases was found to be negligible due to its low thermal conductivity. The loss through the aluminum wall, however, was estimated to be 0.72% of the total power input to the system for the 400 W/m^2 case and 1.22% of the total power input for the 700 W/m^2 case.

2.6 Benchmark Results

The test section walls are designated as follows, and are shown in Fig. 6: The opaque, aluminum wall of the test section (on the $y = 0$ mm plane) is referred to as the "Plate", the wall opposite the Plate (on the $y = 304.8$ mm plane) is the "Top Wall", the wall that lies on the $x = +152.4$ mm plane is referred to as the "Left Wall" and the wall at the $x = -152.4$ mm plane is referred to as the "Right Wall".

The rods are designated by numbers 1-4 starting at the top right corner going counter-clockwise when looking from the test section inlet in the positive z-direction as shown in Fig. 6.

2.6.1 Inflow

Inflow data for both cases are shown in Figs. 17–20. The velocity contour plots (in Figs. 17 and 19) show the $\overline{w}$ velocity component across the inlet of the test section. The arrow indicates the direction of increasing contour levels and the dashed line (at $x = 0$ m) represents the location of the velocity profiles in Figs. 18 and 20 which show all three components of velocity. Turbulence intensity is also plotted with the velocity components along the dashed line and was calculated by

$$I = \frac{\sqrt{\frac{2}{3}k}}{\overline{w}_{\mathrm{bulk}}} \tag{12}$$

where where the turbulence kinetic energy $k = \frac{1}{2}(\overline{u'u'} + \overline{v'v'} + \overline{w'w'})$ and the bulk velocity $\overline{w}_{\mathrm{bulk}}$ is the mean inlet velocity and its value for each case is listed in the figure caption. Turbulence intensity peaks near the walls as the relative magnitude of the stream-wise velocity component decreases, causing a greater impact of the $\overline{u'u'}$ and $\overline{v'v'}$ components of turbulence intensity.

Average turbulence quantities at the test section inlet are presented in Table 4. Here, average turbulent shear stress $\overline{\tau}$ was calculated in the DaVis software [29] by

$$\overline{\tau} = \sqrt{\frac{1}{4}(\overline{v'v'} - \overline{u'u'}) + (\overline{u'v'})^2}. \tag{13}$$

Turbulence dissipation rate was calculated using the standard approximation $\varepsilon \cong C_\mu^{3/4} k^{3/2}/\ell$ where $C_\mu = 0.09$ and the mixing length $\ell = 0.07 D_h$. Likewise, specific turbulence dissipation rate was determine by $\omega = \varepsilon / C_\mu / k$.

Table 4. Average turbulence quantities at the test section inlet. The turbulence model constant $C_\mu = 0.09$ when calculating ε and ω.

	Natural400 Case	Natural700 Case
$\overline{w}_{\text{bulk}}$, [m/s]	0.199±0.002	0.263±0.002
k, [m^2/s^2]	0.00040±0.00004	0.00052±0.00005
$\overline{\tau}$, [m^2/s^2]	0.00007±0.00001	0.00013±0.00001
I	0.0820±0.0039	0.0708±0.0036
ε, [m^2/s^3]	0.00006±0.00007	0.00009±0.00010
ω, [1/s]	1.71±2.01	1.95±2.11

2.6.2 Rod and Wall Temperatures

The non-dimensionalized rod temperature in the stream-wise direction are shown in Figs. 11 and 12 for the Natural400 and Natural700 cases. High thermal conductivity of the aluminum rods resulted in negligible circumferential variation in rod temperature. The rod and wall temperature measurements are found in the RodTemperatures.csv and WallTemperatures.csv files, respectively. The temperature increases in the stream-wise direction as the mixed mean fluid temperature increases as expected with a sharp increase in temperature between points 3 and 4 (at ~ 0.6 m) due to the presence of the grid spacer.

The centerline temperatures for each wall are shown in Figs. 13 and 14. The heat loss from the test section walls due to slightly elevated temperatures was discussed in Section 2.5.

2.6.3 Outlet Fluid Temperatures

Fluid heating is concentrated in the center of the test section directly down-stream of the rod bundle. The 4×4 array of TCs measured the outlet temperature profile and contour plots are shown in Figs. 15 and 16. Outlet temperatures are found in the OutletTemperatures.csv file.

2.6.4 Velocity Profiles

Twelve velocity fields were measured for each heating case at the SRQ locations shown in Figs. 9 and 10. The velocity profiles at each of these locations were extracted from the fields and are plotted

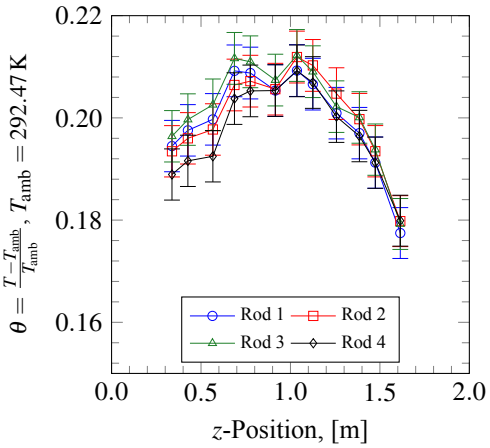

Fig. 11. Rod temperatures in the stream-wise direction for the Natural400 case.

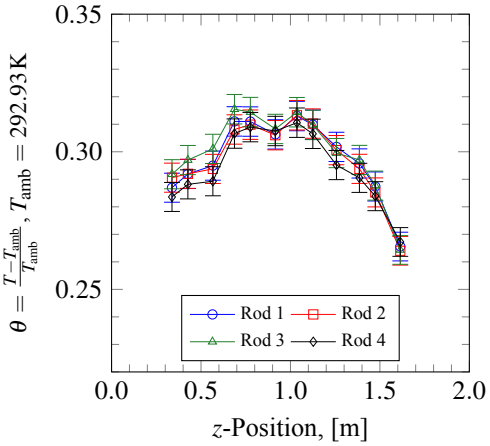

Fig. 12. Rod temperatures in the stream-wise direction for the Natural700 case.

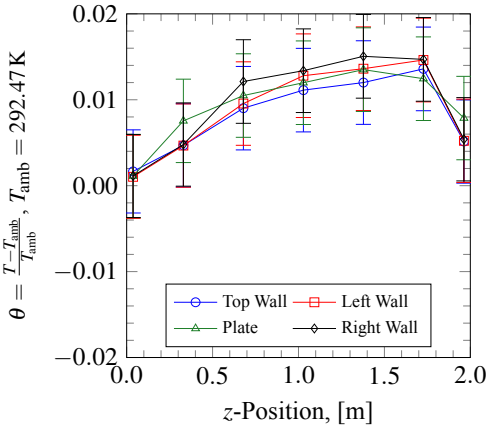

Fig. 13. Wall temperatures in the stream-wise direction for the Natural400 case.

in Figs. 21 and 22 along with the six Reynolds stress components. The mean velocity from each profile w_{bulk} has been subtracted from the stream-wise velocity component for comparison to the other components and its value is shown in each y-axis label. Each figure contains four plots aligned vertically for comparison in the flow-wise direction and the z-position is indicated on each plot area. For the sake of brevity, only the Natural700 case will be presented here. The Natural400 case presented similar SRQ trends as the Natural700 case, differing only by magnitude, and may be found in [1] or in the attached data files.

For the $x = 0$ m plane (lying between the fuel rods) in Fig. 21, the effect of the swirl elements strongly present in the $\overline{u}$ velocity component where $y = 0.154$ m corresponds to the centerline of the fuel rod bundle. The increasing magnitude of w_{bulk} in the flow wise direction is present due to the acceleration of the flow due to buoyancy. The Reynolds stresses in the $z = 0.476$ m and $z = 0.825$ m positions are negligible, however, after entering the transition flow regime the Reynolds stresses increase rapidly as shown in the $z = 1.174$ m and $z = 1.524$ m positions of Fig. 21. This phenomenon is in good agreement with the local Rayleigh number, which indicates that transition to turbulence occurs at approximately half the length of the rod bundle (between the $z = 0.825$ m and $z = 1.174$ m SRQ locations).

The strong through-plane swirl effect of the mixing vanes is visible at all z-locations of the $x = 0$ m plane (Fig. 21) while the in-plane horizontal velocity component, $\overline{v}$, is nearly zero at all z-positions. The normal Reynolds stresses at this x-position are also the only significant contributors to the Reynolds

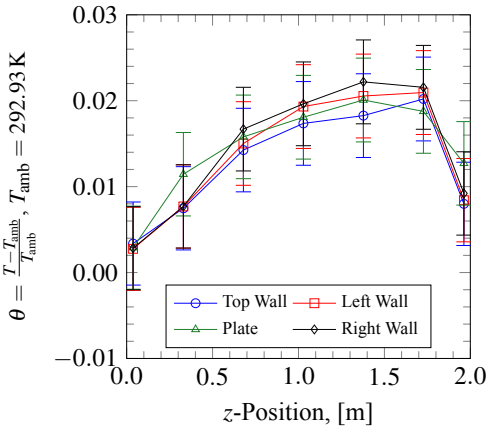

Fig. 14. Wall temperatures in the stream-wise direction for the Natural700 case.

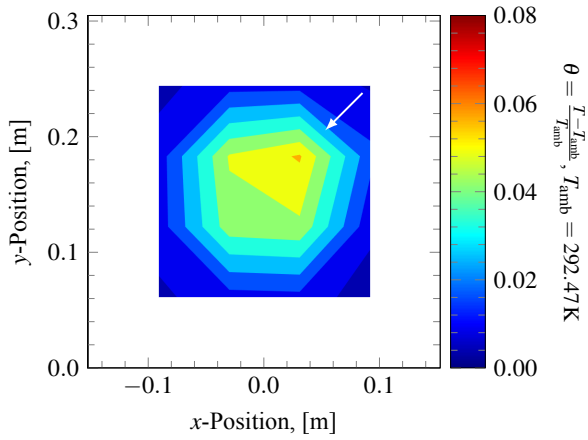

Fig. 15. Outlet fluid temperatures at $z = 2$ m for the Natural400 case. The contour scale begins at $\theta = 0$ and has an increment of 0.008. The arrow indicates the direction of increasing temperature. The TCs were arranged in a 4×4 square grid and were evenly spaced across the test section outlet (61 mm apart in the x and y directions). TC uncertainty in terms of θ was approximately ± 0.0046.

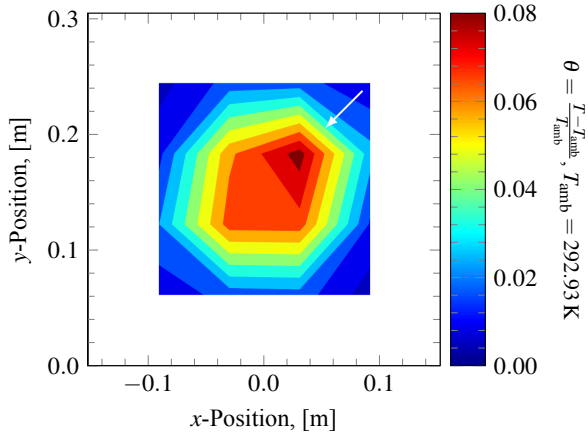

Fig. 16. Outlet fluid temperatures at $z = 2$ m for the Natural700 case. The contour scale begins at $\theta = 0$ and has an increment of 0.008. The arrow indicates the direction of increasing temperature. The TCs were arranged in a 4×4 square grid and were evenly spaced across the test section outlet (61 mm apart in the x and y directions). TC uncertainty in terms of θ was approximately ± 0.0047.

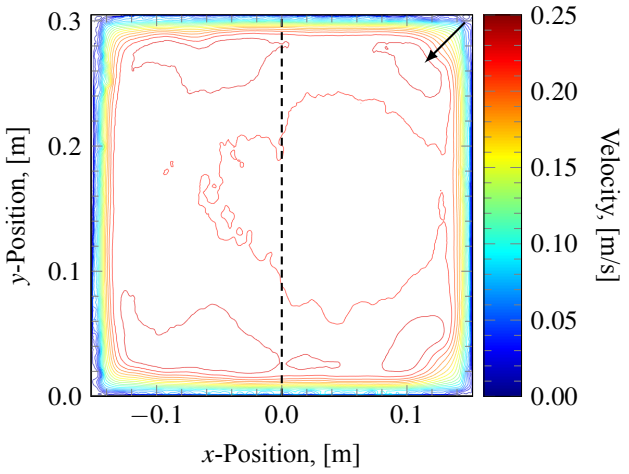

Fig. 17. Contour plot of the test section inflow measurement for the Natural400 case. The first contour level begins at 0 m/s and the increment is 0.0125 m/s. The arrow indicates increasing contour levels and the dashed line represents the location of the line profile in Fig. 18.

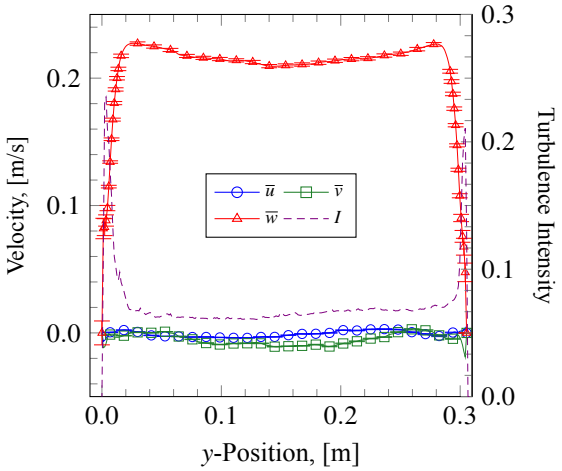

Fig. 18. Inlet velocity profile at the test section centerline ($x = 0$ m) for the Natural400 case. The location of the profile is shown as a dashed line in Fig. 17. The velocity used for calculating turbulence intensity was $\overline{w}_{\text{bulk}}$ =0.1956 m/s.

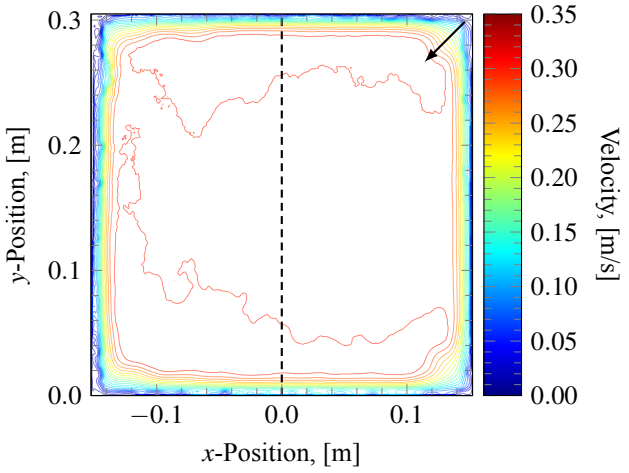

Fig. 19. Contour plot of the test section inflow measurement for the Natural700 case. The first contour level begins at 0 m/s and the increment is 0.0175 m/s. The arrow indicates increasing contour levels and the dashed line represents the location of the line profile in Fig. 20.

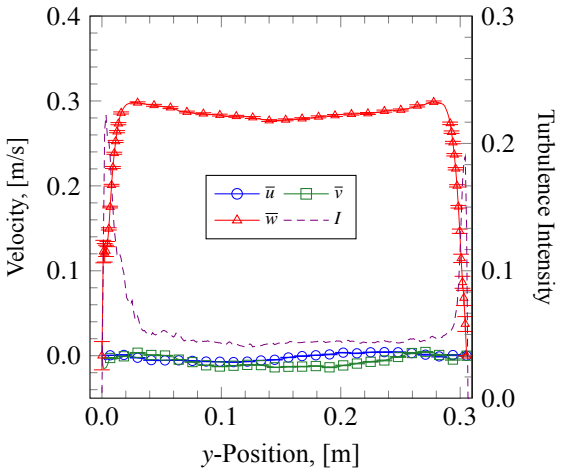

Fig. 20. Inlet velocity profile at the test section centerline ($x = 0$ m) for the Natural700 case. The location of the profile is shown as a dashed line in Fig. 19. The velocity used for calculating turbulence intensity was $\overline{w}_{\text{bulk}}$ =0.2584 m/s.

stress tensor with the Reynolds shear stresses being nearly zero at all z-positions.

The fluid flow on the $x = -0.060$ m plane (just outside the rod bundle) differs greatly from that of the $x = 0$ m plane and is shown in Fig. 22. The fluid acceleration due to the growth of the boundary layer increases less quickly due to the much larger mass of bulk fluid accelerating outside the fuel rod bundle. This results in lower velocity magnitudes overall as evidenced by the magnitude of w_{bulk} when compared to the $x = 0$ m plane. The Reynolds stresses outside the rod bundle also have significantly decreased magnitudes. At the lowest z-location, a slight decrease in stream-wise velocity immediately downstream of the swirl elements is present. The Reynolds stresses in the $z = 0.476$ m and $z = 0.825$ m are nearly zero lying in the laminar flow regime. At $z = 1.174$ m the Reynolds stresses become non-zero near the center of the rod bundle (the left side of the plot) as the bulk fluid velocity also increases most dramatically in this region. Upon reaching the $z = 1.524$ m, turbulence diffuses outward into the flow (toward the right of the x-axis) causing non-zero Reynolds stresses and increased bulk velocity.

The velocity and Reynolds stress SRQ measurements are presented in the attached files as follows. The location of each profile is called out in the filename beginning with "Velocity_" or "ReynoldsStress_" followed by the x and z coordinates of the profile in millimeters. Thus the file "ReynoldsStress_x-60,z1174.csv" contains the profile of Reynolds stresses along the y-direction for all y at $x = -60$ mm and $z = 1174$ mm.

3 CFD Validation Study

3.1 NUMERICAL METHOD

The general purpose CFD solver STAR-CCM+ was used in this work. Second-order upwinding was used for interpolation of variables to cell centers for all transport equations. Pressure-velocity coupling was accomplished using the SIMPLE procedure. Solution residuals were reduced 3 or more orders of magnitude for all equations.

Given the relatively large variation in fluid temperatures inherent in the problem, the molecular viscosity and thermal conductivity were specified as functions of temperature. In particular, the molecular viscosity was computed using Sutherland's law, and a polynomial fit was used to define the thermal conductivity. In addition, density was computed using the incompressible ideal gas law. Material properties for the aluminum rods were set to constant values.

Two turbulence models were employed; a two-layer realizable model, and a two-layer, linear pressure strain differential Reynolds stress model (RSM). In the two-layer approach, near the wall the turbu-

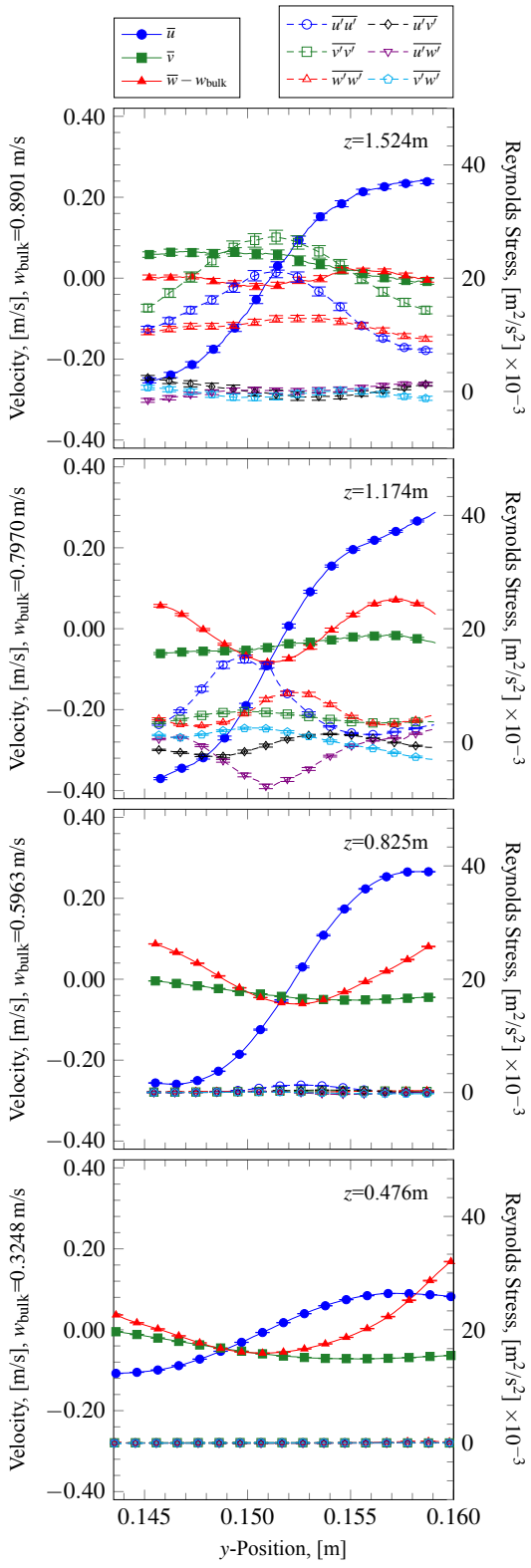

Fig. 21. Velocity profile along y-direction for $x = 0$ m at four z-positions indicated on each plot for the Natural700 case.

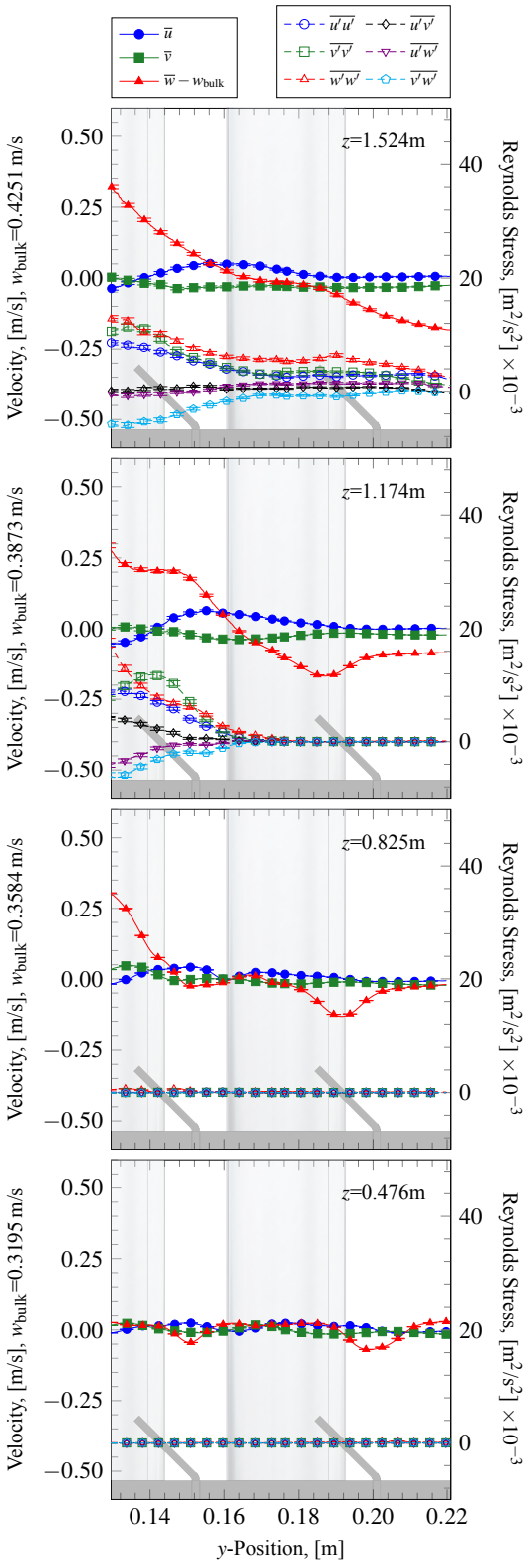

Fig. 22. Velocity profile along y-direction for $x = -0.06$ m at four z-positions indicated on each plot for the Natural700 case. The relative locations of the swirl elements in the y-position (not to scale in z) are shown in the background of each figure.

lence dissipation rate and turbulence viscosity are specified as a function of distance from the wall [36]. In particular, the dissipation rate is specified as:

$$\varepsilon = \frac{k^{3/2}}{l_\varepsilon} \tag{14}$$

where l_e is a length scale and k is the turbulent kinetic energy. For comparative purposes, two different near wall two-layer formulations have been used in this work; the Wolfstein model [37] which is primarily used for shear driven flows, and the Xu model [38] which is primarily used for buoyancy driven flows; the purpose being to assess the importance of the length scale and turbulent viscosity prescriptions in the near wall region. For the Wolfstein model the length scale is defined as:

$$l_\varepsilon = \kappa C_\mu^{-3/4} y \left[1 - exp\left(-\frac{Re_y}{A_\varepsilon}\right)\right], \tag{15}$$

where $A_\varepsilon = 2\kappa C_\mu^{-3/4}$, $C_\mu = 0.09$ and $\kappa = 0.42$. The turbulent viscosity is given as:

$$\mu_t = \mu Re_y C_\mu^{1/4} \kappa \left[1 - exp\left(-\frac{Re_y}{70}\right)\right]. \tag{16}$$

The length scale for the Xu model is given as:

$$l_\varepsilon = \frac{8.8y}{1 + 10/y_v^* + 5.15x10^{-2} y_v^*} \frac{1}{\sqrt{\overline{v^2}/k}}, \tag{17}$$

and the turbulent viscosity is formulated as:

$$\mu_t = \mu \frac{0.544 y_v^*}{1 + 5.025x10^4 {y_v^*}^{1.65}}. \tag{18}$$

In addition,

$$\overline{v^2}/k = 7.19x10^{-3} Re_y - 4.33x10^{-5} Re_y^2 + 8.8x10^{-8} Re_y^3 \tag{19}$$

and

$$y_v^* = Re_y \sqrt{\overline{v^2}/k}. \tag{20}$$

Fig. 23. Tunnel Configuration

3.2 Computational Geometry

The computational geometry represents a model of an experimental configuration that consisted of an array of four heated rods spanning the majority of the length of the 2-meter-long tunnel test sectio. Within the tunnel, each of the four rods contained instrumentation to measure surface temperatures at several stream wise locations. The rods were nickel coated to minimize radiative heat transfer. Grid spacers with swirling vanes were also incorporated. A photograph of the experimental arrangement is shown in Fig.23.

Shown in Figs. 24 and 25 are side and top views of the computational geometry, respectively. The location of the rods and spacers relative to the inlet and exit planes is shown in Fig. 24. The location of the swirler vanes is shown in Fig. 25. Note the orientation of the vanes precludes the existence of a symmetry plane. In terms of the overall scale, the length of the computational domain, from inlet to exit, is 3.6129 m and the width in the square test section area is 0.762m.

3.3 Boundary Conditions

The flow through the tunnel is purely buoyancy driven. Hence, consistent with the experimental configuration, heat flux boundary conditions of 2,333 W/m^2 were specified along the inner surface of the annular rods. This corresponds to a heat flux of 700W/m^2 along the outer surface of the rods. At the inlet, a stagnation boundary condition in which Bernoulli's equation is used to relate total pressure, static pressure, and velocity magnitude was specified. The condition is intended to model the conditions in an imaginary upstream plenum in which the flow is completely at rest. However, the experimental facility included screens, honeycombs, and a heat exchanger at the entrance to the tunnel with a measured pressure loss coefficient of $K = 166$. To take this flow restriction into account, a pressure drop option was implemented such that the pressure loss across the inlet boundary was specified as $\Delta p = 0.5K\rho\left|v^2\right|$. Supplemental calculations were completed to demonstrate the importance of including this pressure loss. Inlet turbulence conditions on k and were derived from a turbulence intensity of 1 percent, and a turbulence viscosity ratio of 10. The inlet (and reference) temperature was fixed at 293K. The boundary condition at the exit plane was specified as the static pressure. An adiabatic condition was specified along the outer tunnel walls. This is not completely consistent with the experimental facility as those walls were not insulated; however the estimated heat transfer rates are quite low. Finally, we note that

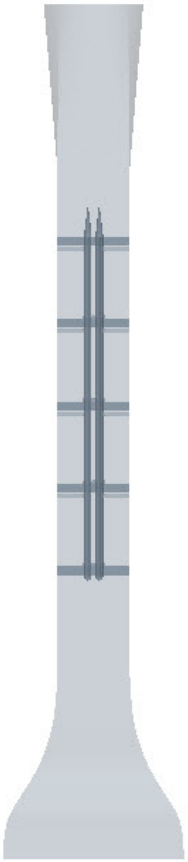

Fig. 24. Side view of computational domain.

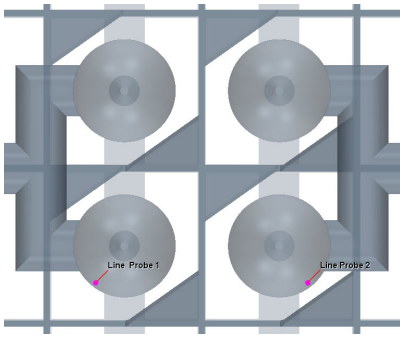

Fig. 25. Top view ($x-y$ plane) showing line plot locations on rod 1 and rod 2, denoted as Line Probe 1 and Line Probe 2, respectively, and swirler vane locations.

the placement of the swirler vanes as shown in Fig. 25 preclude the implementation of a symmetry plane boundary condition along the domain centerline.

3.4 Numerical Results

We first examined the influence of the inlet pressure drop due to flow conditioning devices on the overall mass flow rate through the domain. In particular, simulations were completed with the pressure loss coefficient K set to either 166 or 0. The results for both turbulence models, along with experimental results are shown in Table 5. The computational results indicate a decrease in mass flow rate of approximately 30% when the influence of the flow conditioning devices is included. The numerical results for

which the flow conditioning effects were included agree quite well with the experimentally determined flow rate.

This significant decrease in flow rate would certainly be expected to alter the heat transfer characteristics within the domain. The extent of this is demonstrated in Fig. 26 which shows the influence of the inlet pressure losses on the predicted wall temperatures for rod 1. Clearly, the inclusion of the flow conditioning effects results in a significant increase in rod wall temperature. Consequently, subsequent results all include the pressure loss across the boundary.

The primary interest in this work is to investigate the performance of the turbulence models in predicting the rod wall temperatures. Consequently, we present in Fig. 27 computed and experimental axial temperature distributions along rods 1 and 2. The radial locations at which the results are presented are indicated in Fig. 25, labeled as line probe 1 and line probe 2 (corresponding to rods 1 and 2, respectively). Results for two-layer implementations of both and Reynolds stress models are shown. In addition, within the two-layer models, results for both shear driven (Wolfstein model) and buoyancy driven (Xu model) formulations are presented for both the and Reynolds stress models. The results indicate slight differences in the temperature distributions along rods 1 and 2 for a given turbulence model. This difference is slightly more pronounced for the RSM results than the results, with rod 2 at slightly higher predicted temperatures. The slightly higher temperatures for rod 2 are attributed to the location of the swirler vanes; in particular, the location of the inner vanes which are situated in a relatively hot fluid

Table 5. Mass flow rates through domain.

Experiment	$k-\varepsilon$ w/. blockage	$k-\varepsilon$ w/o. blockage	RSM w/. blockage	RSM w/o. blockage
0.025 kg/s	0.0272kg/s	0.037kg/s	0.0279kg/s	0.037 kg/s

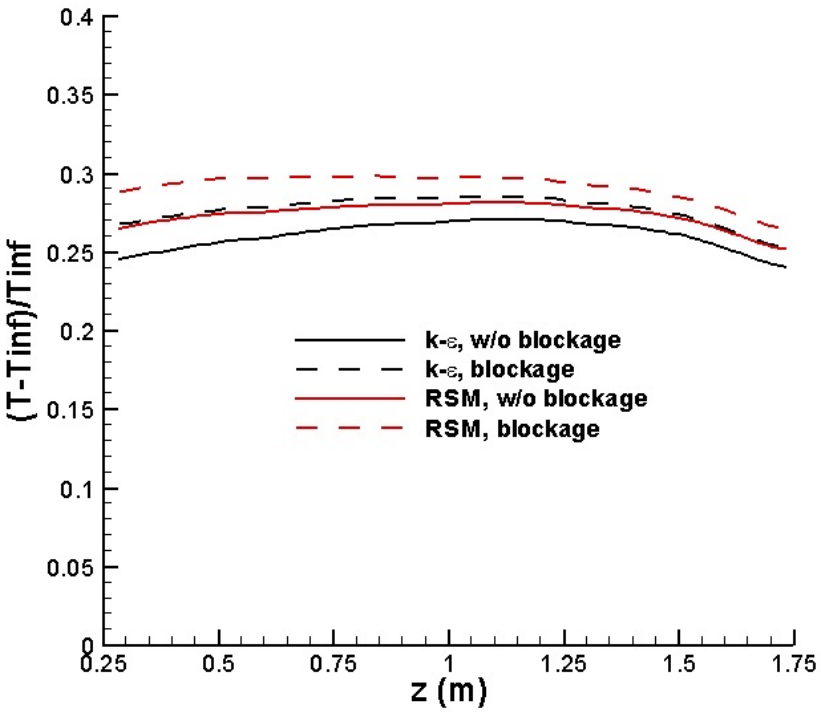

Fig. 26. Influence of inlet pressure losses on computed temperatures for rod 1.

stream (see Fig. 25) and hence are less effective as a device to enhance heat transfer. We suspect the RSM shows slightly greater differences between rods than the due to its ability to maintain the swirling motion to a greater extent along the rod; i.e., it is less dissipative. In comparison with the experimental results both the RSM and models when implementing the Xu [38] two-layer model perform quite well, with the RSM predictions slightly higher than the predictions. However, when the Wolfstein [37] two-layer model is implemented, both RSM and significantly over-predict the wall temperatures. The above results were computed using a mesh that consisted of 7.6 million cells. The adequacy of this discretization is discussed next.

Grid convergence studies for and RSM model predictions for rod 1 are shown in Fig. 28. Solutions were obtained on three mesh levels consisting of 3.9, 7.6, and 14.7 million cells. Clustering toward the solid surfaces was such that the average value of y^+ on both the rods and spacers for the 7.6 million cell case was ≈ 0.6. Results indicate that the wall temperature results for the mid-level mesh are adequately grid resolved for both and RSM models.

In addition to rod wall temperatures, experimental velocity data was available at selected locations. The numerical results are compared against these experimental data in Figs. 29-36. In particular, experimental data is available in the y-direction along eight line segments. The z (vertical) location of these lines is indicated in Fig. 37 on constant z-planes 0.476m, 0.825m, 1.174m, and 1.524m, where we have also plotted contours of velocity magnitude. Note that these planes lie midway between grid spacers. The x-locations and the extent of the available data in the y-direction is shown in Fig. 38 where $x = 0$ lies exactly midway between the cylinders and $y = 0$ corresponds to the tunnel wall. The temperature contours in Fig. 38 which are shown on the z=1.524m plane reveal a lack of symmetry in the flow which is due to the influence of the swirler vanes.

We compare in Figs. 29-32 profiles of velocity magnitude at $z = 0.476$m, 0.825m, 1.174m, and

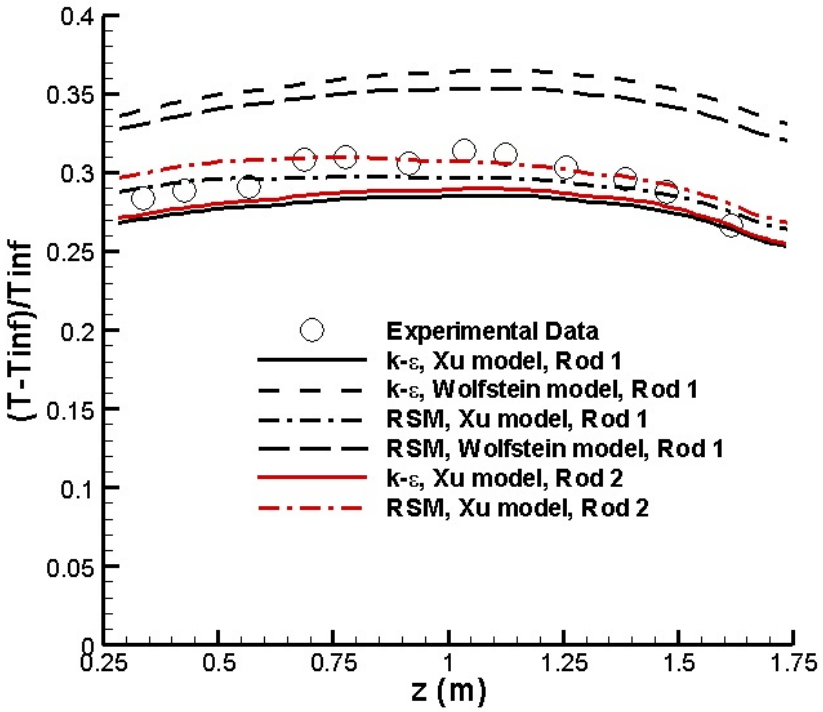

Fig. 27. Comparison between predicted and experimental rod temperatures.

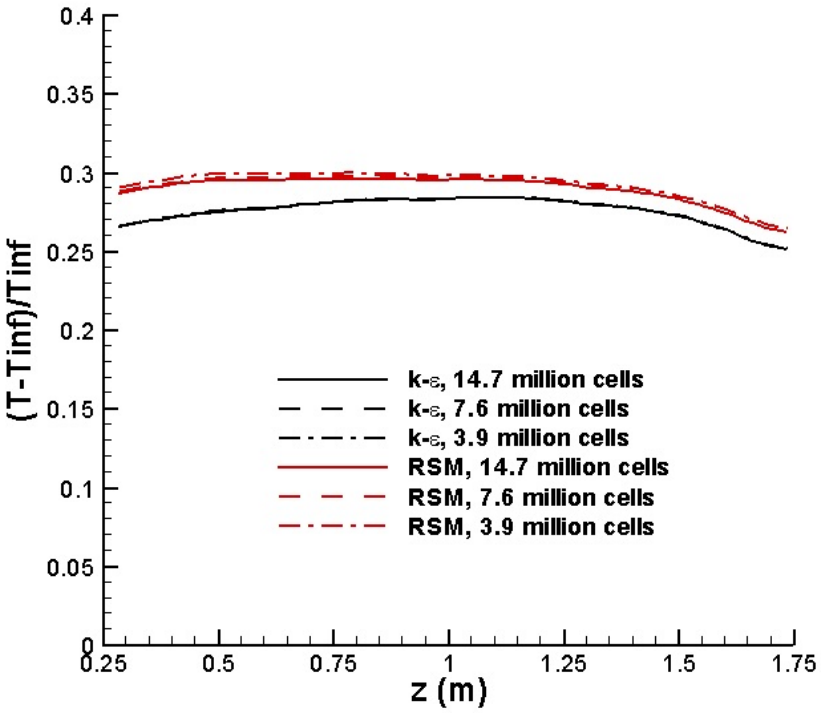

Fig. 28. Grid resolution study results for rod 1.

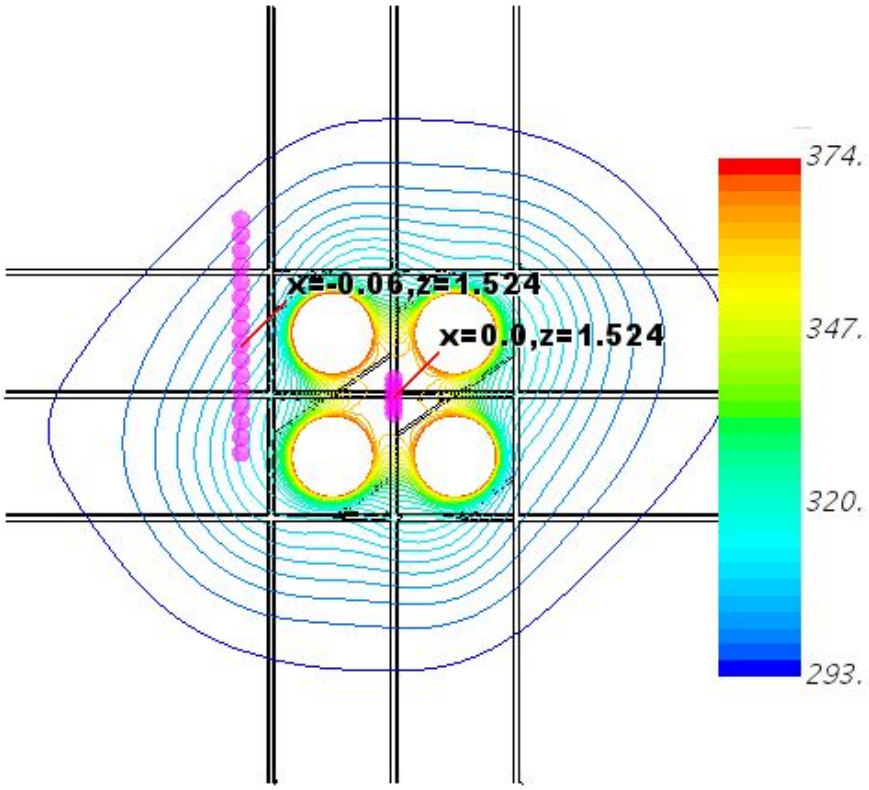

Fig. 29. Comparison between experimental and predicted velocity magnitude at $x = 0.0$m, $z = 0.476$m

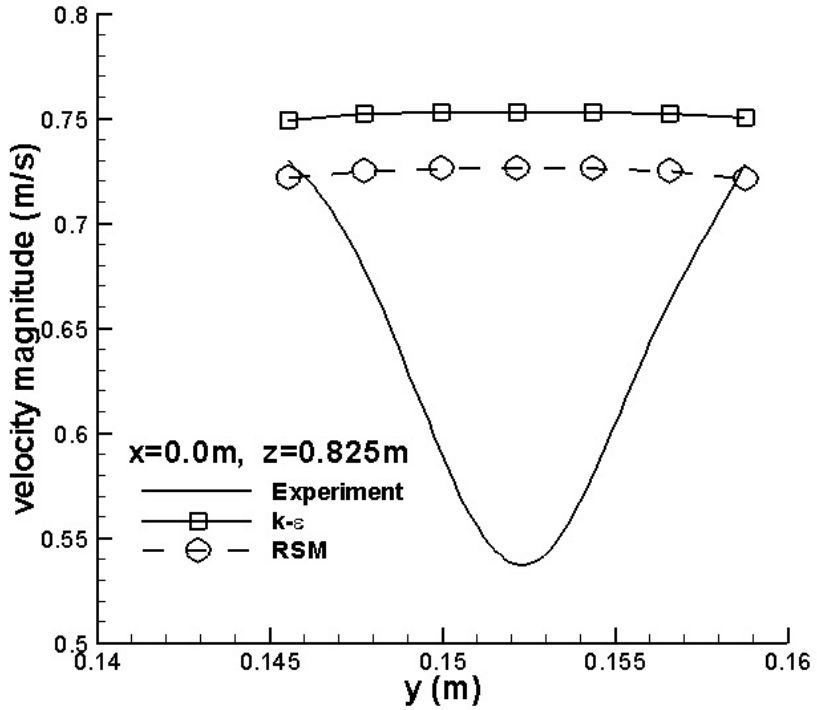

Fig. 30. Comparison between experimental and predicted velocity magnitude at $x = 0.0$m, $z = 0.825$m.

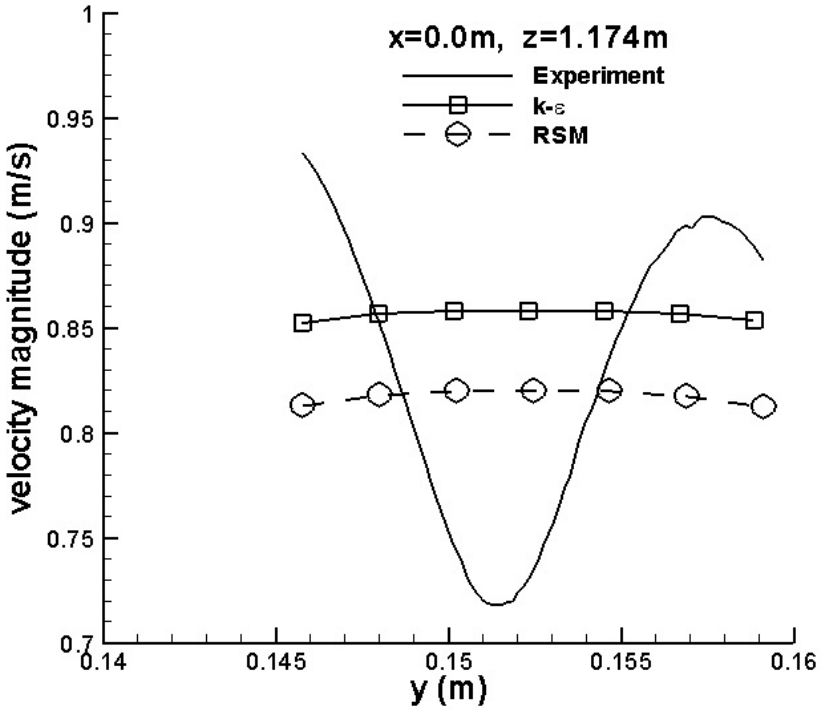

Fig. 31. Comparison between experimental and predicted velocity magnitude at $x = 0.0$m, $z = 1.147$m.

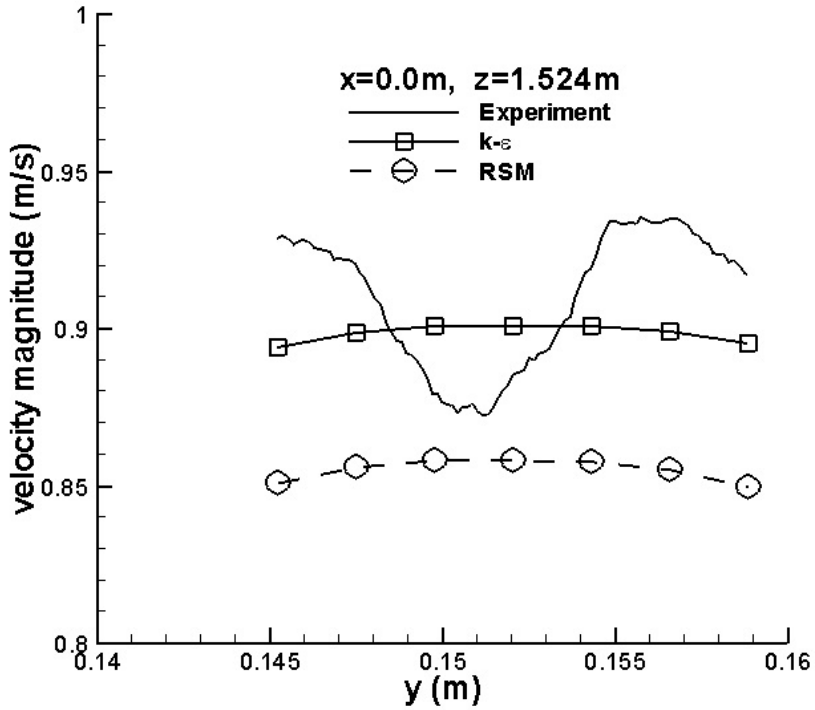

Fig. 32. Comparison between experimental and predicted velocity magnitude at $x = 0.0$m, $z = 1.524$m.

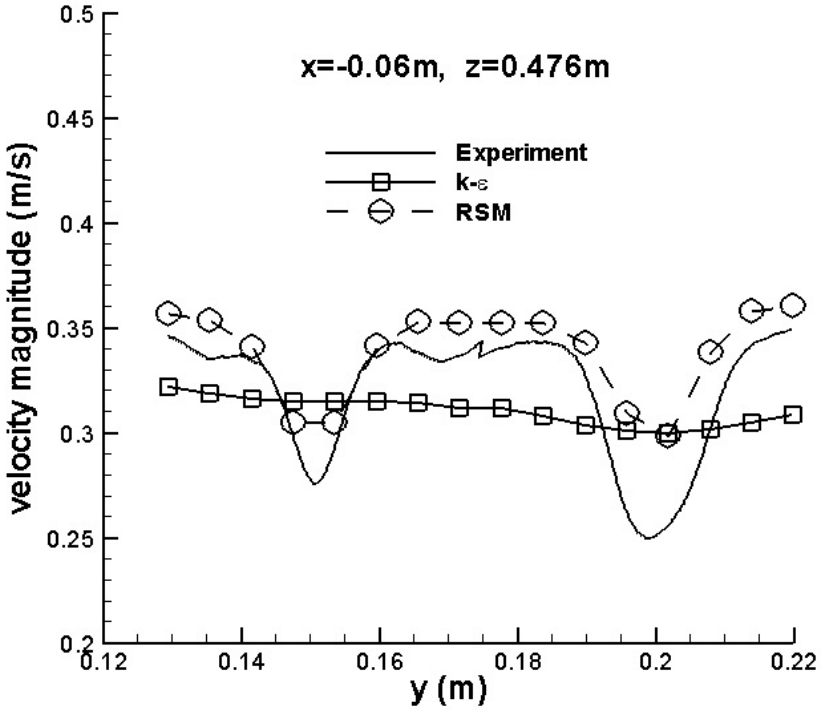

Fig. 33. Comparison between experimental and predicted velocity magnitude at $x = -0.06$m, $z = 0.476$m.

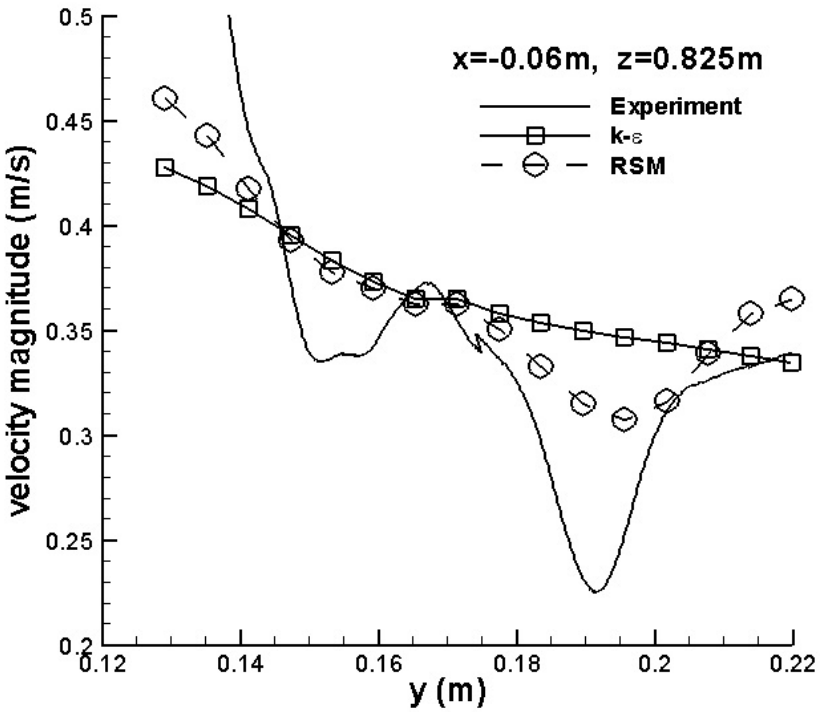

Fig. 34. Comparison between experimental and predicted velocity magnitude at $x = -0.06$m, $z = 0.825$m.

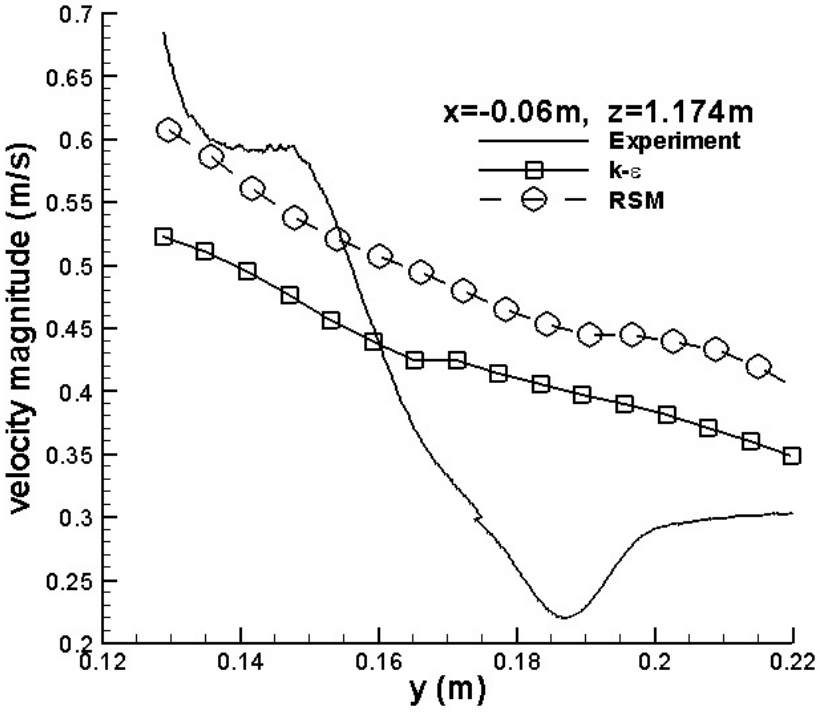

Fig. 35. Comparison between experimental and predicted velocity magnitude at $x = -0.06$m, $z = 1.174$m.

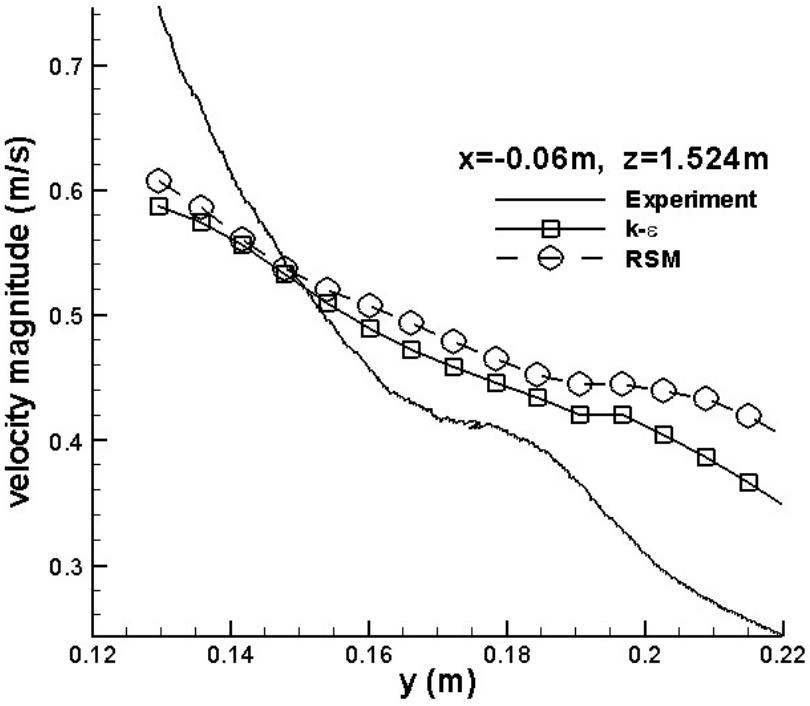

Fig. 36. Comparison between experimental and predicted velocity magnitude at $x = -0.06$m, $z = 1.524$m.

1.524m, respectively. In addition, at $x = 0.0$m these lines are along the centerline of the domain, and are above grid spacers. The experimental results clearly reveal a local minimum in the velocity profile at $y \approx 0.165$m. This minimum represents the wake that has developed downstream from a 0.002m wide spacer. The numerical results do not retain this wake region. We attribute this primarily to the relatively low mesh resolution in the narrow wake region. The symbols for the numerical results indicate that resolution of the wake region midway between vertical spacers is limited to about 6 cells. This was likely too coarse to maintain the velocity defect of the wake. However, the wake region is quite narrow, and attempting to resolve these wakes would require more computational resources than available. Fortunately, the wall temperature predictions shown in Figs. 27-28 indicate that it is not necessary to resolve all flow field details to obtain accurate predictions of wall temperatures.

In a similar manner, line plots of velocity magnitude at are shown in Figs. 33-36. These results are only slightly improved from those at $x = 0.0$m. The predictions in best agreement with experiment occur at the z=0.476m level. The two local minimums in velocity magnitude that occur adjacent to the northwest edges of the cylinders are reasonably well predicted by the Reynolds stress model. The model does not predict these minimums. At $z = 0.825$m, the RSM predicts the existence of the 2nd local minimum only. At locations $z = 1.174$m and 1.542m, neither the RSM nor the model indicate local minimums.

Global views of the flowfield in terms of velocity magnitude are shown in Figs. 39-40 for the and RSM models, respectively. From this perspective, the flowfields predicted by the two models are very similar, with the model showing very slight increase in maximum velocity near the outlet plane. Temperature contours for the two models are shown on the same $y-z$ plane in Figs. 41-42. Again, results are very similar with maximum temperatures for the RSM slightly above those predicted by the model.

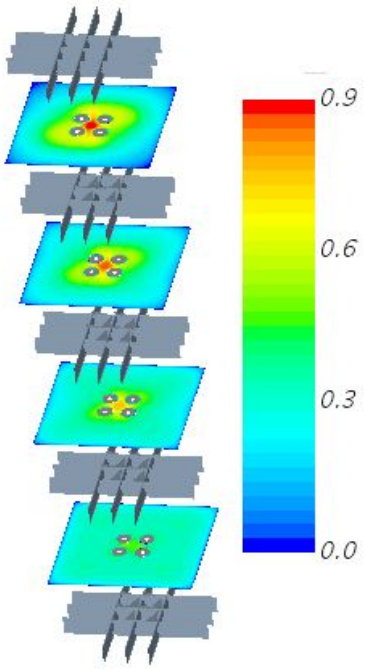

Fig. 37. Contours of velocity magnitude at constant z-planes 0.476m, 0.825m, 1.174m, and 1.524m, corresponding to z locations in Figs. 30 to 37. Spacers shown for reference purposes.

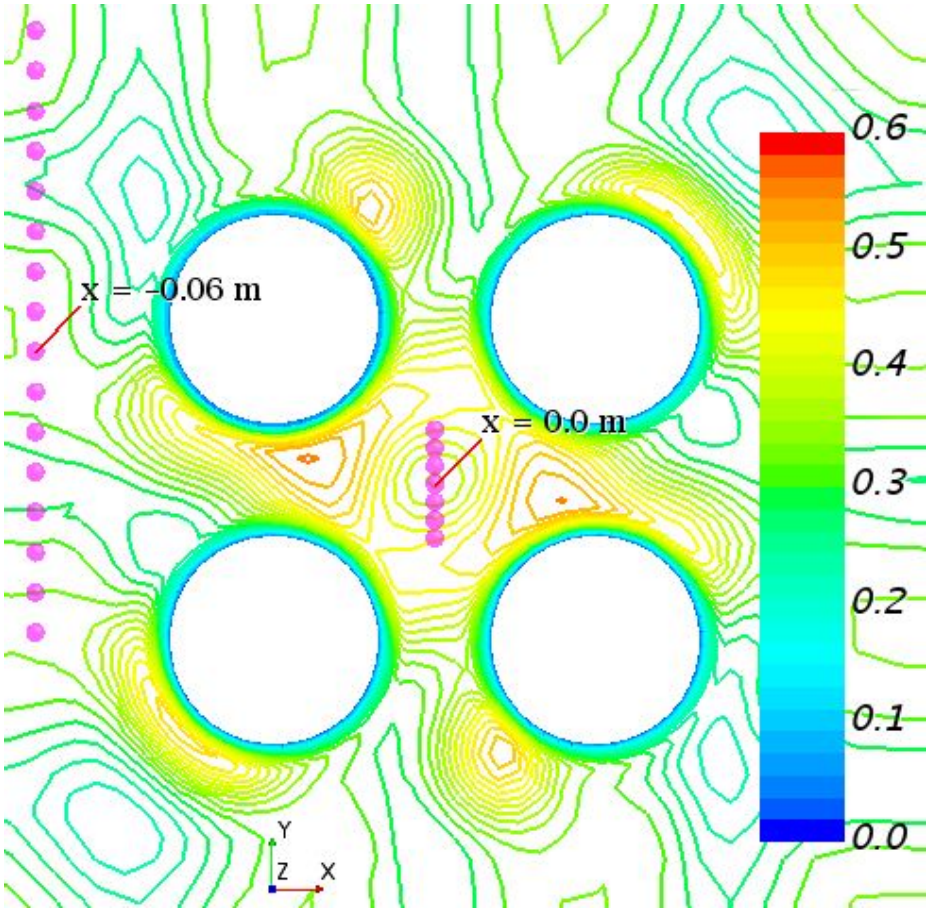

Fig. 38. Locations in the $x-y$ plane at $x = 0$m and $x = -0.06$m for line plots shown in Figs. 30 to 37, with spacers and contours of temperature (K) on the $z = 1.524$m plane superimposed.

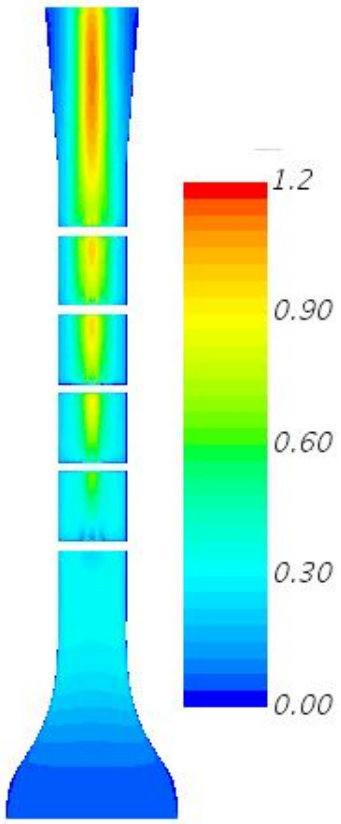

Fig. 39. Contours of velocity magnitude for the model on a $y - z$ plane at $x = 0$.

3.5 Summary of Validation Study

The Reynolds-averaged Navier-Stokes equations were solved to predict the flow over an array of vertical, heated cylinders. Results using both and differential Reynolds stress models were examined. For each model, a two-layer formulation was employed. In addition, results for both Wolfstein [37] and Xu [38] two-layer formulations were examined. Wall temperatures and velocity profiles were compared against existing experimental data. In terms of wall temperatures, the Xu model was specifically developed for buoyancy driven flows showed much better agreement with the experimental results than those computed using the Wolfstein model. In particular, results using the Wolfstein model significantly over predicted the wall temperatures. For both the Xu and Wolfstein models, the model predicted slightly higher wall temperatures than the Reynolds stress model. Computed velocity profiles were compared against experimental data at 8 locations. In general, the comparisons were not particularly favorable, likely due to the difficulty in resolving the narrow wake structures behind the rod spacers. However, this inability to accurately capture the spacer wake region does not appear to have adversely affected the ability of the models to accurately predict the wall temperatures. Overall flowfields, as revealed in Figs. 39-42, revealed only minor differences in the model predictions.

Conclusion

This study has presented experiments and an accompanying validation study that were performed for steady-state natural convection in nuclear fuel rod bundles under two constant heat flux surface conditions (400 W/m^2 and 700 W/m^2). The geometry, BCs and SRQs are available for download and use for CFD model validation. Stereoscopic PIV was used for unintrusive velocity measurements. The BCs and SRQs considered are listed in Table 1. Uncertainties for all measured and derived quantities

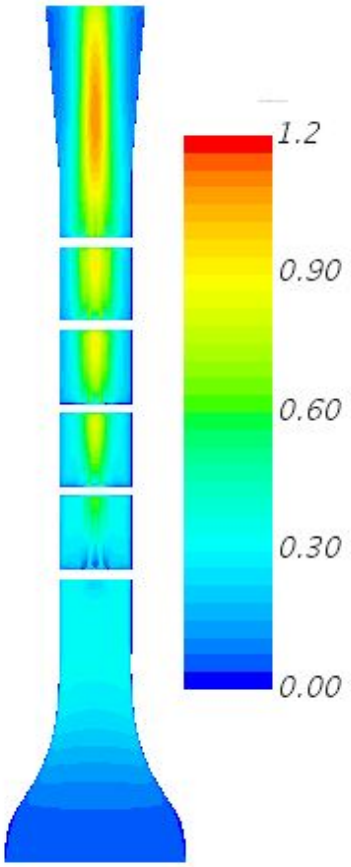

Fig. 40. Contours of velocity magnitude for the RSM model on a $y-z$ plane at $x=0$.

were also calculated and are included in each of the attached files. Tight coupling of fluid properties and flow characteristics, along with a flow driven by thermal BCs rather than inflow, make natural convection difficult to simulate. These data provide a benchmark case that may be used to validate CFD models.

References

[1] Jones, K. L., 2016. *Benchmark Experiments for Natural Convection in Nuclear Fuel Rod Bundles*. PhD Dissertation, Utah State University.

[2] U.S. Department of Defense, 1996. *Verification, Validation and Accreditation (VV&A) Recommended Practices Guide*. Defense Modeling and Simulation Office, Office of the Director of Defense Research and Engineering, Nov.

[3] AIAA, 1998. *Guide for the Verification and Validation of Computational Fluid Dynamics Simulations*, vol. G-077-1998. AIAA.

[4] ASME, 2009. *Standard for Verification and Validation in Computational Fluid Dynamics and Heat Transfer*. American Society of Mechanical Engineers.

[5] Oberkampf, W. L., and Roy, C. J., 2010. *Verification and Validation in Scientific Computing*. Cambridge University Press.

[6] Roache, P. J., 2009. *Fundamentals of Verification and Validation*. Hermosa Publishing.

[7] Oberkampf, W. L., and Trucano, T. G., 2000. "Validation methodology in computational fluid dynamics". In Fluids 2000, AIAA.

[8] Oberkampf, W. L., and Trucano, T. G., 2002. *Verification and Validation in Computational Fluid Dynamics*. Cambridge University Press.

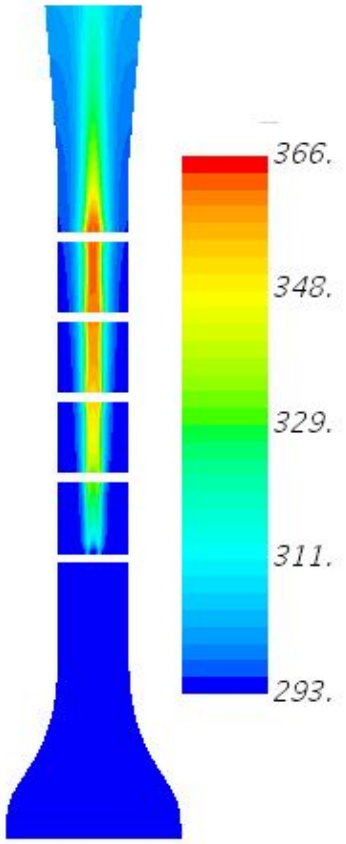

Fig. 41. Temperature contours for the model on a $y-z$ plane at $x=0$.

[9] Oberkampf, W. L., and Barone, M. F., 2006. "Measures of agreement between computation and experiment: Validation metrics". Journal of Computational Physics, **217** (1) , pp. 5–36.

[10] Oberkampf, W. L., and Smith, B., 2014. "Assessment criteria for computational fluid dynamics validation benchmark experiments". In 52nd Aerospace Sciences Meeting, vol. 205, American Institute of Aeronautics and Astronautics, pp. 1–27.

[11] Kays, W., Crawford, M., and Weigand, B., 2005. *Convective Heat and Mass Transfer*, 4th ed. McGraw-Hill Higher Education, Boston, Massachusetts.

[12] De Vahl Davis, G., 1983. "Natural convection of air in a square cavity: A benchmark numerical solution". International Journal for Numerical Methods in Fluids, **3** (3) May , pp. 249–264.

[13] Leong, W., Hollands, K., and Brunger, A., 1998. "On a physically-realizable benchmark problem in internal natural convection". International Journal of Heat and Mass Transfer, **41** (23) Dec , pp. 3817–3828.

[14] Leong, W. H., Hollands, K. G. T., and Brunger, A. P., 1999. "Experimental Nusselt numbers for a cubical-cavity benchmark problem in natural convection". International Journal of Heat and Mass Transfer, **42** (11) Jun , pp. 1979–1989.

[15] Mamun, M. A. H., Leong, W. H., Hollands, K. G. T., and Johnson, D. A., 2003. "Cubical-cavity natural-convection benchmark experiments: An extension". International Journal of Heat and Mass Transfer, **46** (19) Sep , pp. 3655–3660.

[16] Ampofo, F., and Karayiannis, T., 2003. "Experimentalbenchmark data for turbulent natural convection in an air filled square cavity". International Journal of Heat and Mass Transfer, **46** (19) Sep , pp. 3551–3572.

[17] Betts, P. L., and Bokhari, I. H., 2000. "Experiments on turbulent natural convection in an enclosed

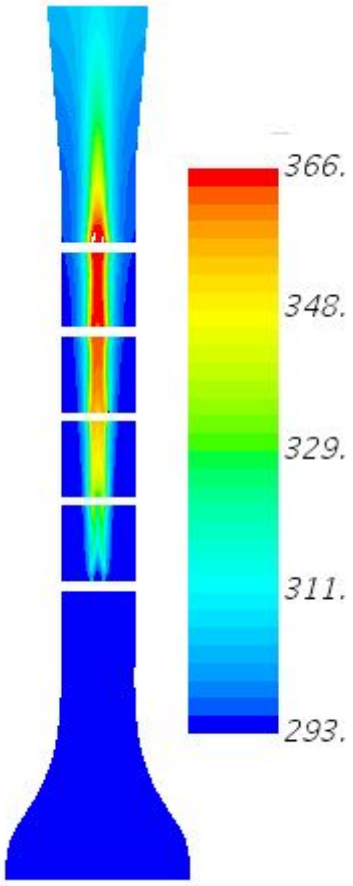

Fig. 42. Temperature contours for the RSM model on a $y-z$ plane at $x=0$.

tall cavity". International Journal of Heat and Fluid Flow, **21** (6) Dec , pp. 675–683.

[18] Tian, Y., and Karayiannis, T., 2000. "Low turbulence natural convection in an air filled square cavity". International Journal of Heat and Mass Transfer, **43** (6) Mar , pp. 849–866.

[19] Rafique, M., Ahmad, I., Basit, M. A., Begum, R., Aziz, W., Farooq, M., and Qureshi, K. R., 2011. "Numerical simulations of natural convection heat transfer along a vertical cylinder". International Journal of Numerical Methods for Heat and Fluid Flow, **21** (1) , pp. 112–130.

[20] Davis, L. P., and Perona, J. J., 1973. "Development of free convection axial flow through a tube bundle". International Journal of Heat and Mass Transfer, **16** (7) July , pp. 1425–1438.

[21] Krishna, D. J., Thansekhar, M. R., Venkateshan, S. P., Basak, T., and Das, S. K., 2010. "Natural convection in a partially heat generating rod bundle inside an enclosure". Journal of Heat Transfer, **132** (10) , pp. 1–11.

[22] McCann, R. A., 1980. "Thermohydraulic analysis of a spent fuel assembly contained within a canister". In ASME Winter Annual Meeting, pp. 91–99.

[23] Koenig, J. F., and Buchanan, T. N., 1979. Temperatures of EBR-II subassemblies in air or argon without forced cooling. Tech. rep., Idaho National Laboratory.

[24] Driesen, G. E., Moran, D. F., Sherba, P. S., and Steffen, R. J., 1980. "Heat transfer associated with dry storage of spent LWR fuel". In ASME Winter Annual Meeting, pp. 9–18.

[25] Kähler, C., 2003. "General design and operating rules for seeding atomisers". In 5th International Symposium on Particle Image Velocimety, no. 3207.

[26] Wen, C.-D., and Mudawar, I., 2002. "Experimental investigation of emissivity of aluminum alloys and temperature determination using multispectral radiation thermometry (MRT) algorithms".

Journal of Materials Engineering and Performance, **11** (October) , pp. 551–562.
[27] Gustavsen, A., and Berdahl, P., 2003. "Spectral emissivity of anodized aluminum and the thermal transmittance of aluminum window frames". Nordic Journal of Building Physics, **3** (1970) , pp. 1–12.
[28] LaVision GmbH, 2015. *FlowMaster Product Manual, Item Number: 1105011-4*. LaVision GmbH, Anna-Vandenhoeck-Ring 19, D-37081 Göttingen, Germany, Mar.
[29] LaVision GmbH, 2015. *DaVis Software ver. 8.2.3*. LaVision GmbH, Anna-Vandenhoeck-Ring 19, D-37081 Göttingen, Germany, Mar.
[30] Warner, S. O., and Smith, B. L., 2014. "Autocorrelation-based estimate of particle image density for diffraction limited particle images". Measurement Science and Technology, **25** (6) Apr , p. 065201.
[31] Coleman, H. W., and Steele, W. G., 2009. *Experimentation, Validation, and Uncertainty Analysis for Engineers*, 3rd ed. John Wiley and Sons, Hoboken, NJ.
[32] Wieneke, B., and Prevost, R., 2014. *DIC Uncertainty Estimation from Statistical Analysis of Correlation Values*. Springer, pp. 125–136.
[33] Wieneke, B., and Sciacchitano, A., 2015. "PIV uncertainty propagation". In The 11th International Symposium on Particle Image Velocimetry–PIV15, p. 38.
[34] Touloukian, Y. S., 1970. *Thermophysical Properties of Matter*. Purdue University. Thermophysical Properties Research Center.
[35] Churchill, S. W., and Chu, H. H., 1975. "Correlating equations for laminar and turbulent free convection from a vertical plate". International Journal of Heat and Mass Transfer, **18** (11) Nov , pp. 1323–1329.
[36] Rodi, W., 1991. "Experience with tow-layer models combining the model with a one-equation model near the wall". In 29th Aerospace Sciences Meeting, AIAA.
[37] Wolfshtein, M., 1969. "The velocity and temperature distribution in one-dimensional flow with turbulence augmentation and pressure gradient". International Journal of Heat and Mass Transfer, **12** (3) , pp. 301–318.
[38] Xu, W., Chen, Q., and Nieuwstadt, F., 1998. "A new turbulence model for near-wall natural convection". International Journal of Heat and Mass Transfer, **41** (21) , pp. 3161–3176.